SMAI-JCM
SMAI Journal of Computational Mathematics

Hybrid Finite-Volume-Particle Method for Dusty Gas Flows

Alina Chertock, Shumo Cui & Alexander Kurganov

Volume 3 (2017), p. 139-180.
<http://smai-jcm.cedram.org/item?id=SMAI-JCM_2017__3__139_0>

© Société de Mathématiques Appliquées et Industrielles, 2017
Certains droits réservés.

cedram
Article mis en ligne dans le cadre du
Centre de diffusion des revues académiques de mathématiques
http://www.cedram.org/

creative commons
BY NC ND

SMAI Journal of Computational Mathematics
Vol. 3, 139-180 (2017)

Hybrid Finite-Volume-Particle Method for Dusty Gas Flows

Alina Chertock [1]
Shumo Cui [2]
Alexander Kurganov [3]

[1] Department of Mathematics, North Carolina State University, Raleigh, NC 27695, USA
E-mail address: chertock@math.ncsu.edu
[2] Department of Mathematics, Temple University, Philadelphia, PA 19122, USA
E-mail address: shumo.cui@temple.edu
[3] Department of Mathematics, Southern University of Science and Technology of China, Shenzhen, 518055, China and Mathematics Department, Tulane University, New Orleans, LA 70118, USA
E-mail address: kurganov@math.tulane.edu.

Abstract. We first study the one-dimensional dusty gas flow modeled by the two-phase system composed of a gaseous carrier (gas phase) and a particulate suspended phase (dust phase). The gas phase is modeled by the compressible Euler equations of gas dynamics and the dust phase is modeled by the pressureless gas dynamics equations. These two sets of conservation laws are coupled through source terms that model momentum and heat transfers between the phases. When an Eulerian method is adopted for this model, one can notice the obtained numerical results are typically significantly affected by numerical diffusion. This phenomenon occurs since the pressureless gas equations are nonstrictly hyperbolic and have degenerate structure in which singular delta shocks are formed, and these strong singularities are vulnerable to the numerical diffusion.

We introduce a low dissipative hybrid finite-volume-particle method in which the compressible Euler equations for the gas phase are solved by a central-upwind scheme, while the pressureless gas dynamics equations for the dust phase are solved by a sticky particle method. The obtained numerical results demonstrate that our hybrid method provides a sharp resolution even when a relatively small number of particle is used.

We then extend the hybrid finite-volume-particle method to the three-dimensional dusty gas flows with axial symmetry. In the studied model, gravitational effects are taken into account. This brings an additional level of complexity to the development of the finite-volume-particle method since a delicate balance between the flux and gravitational source terms should be respected at the discrete level. We test the proposed method on a number of numerical examples including the one that models volcanic eruptions.

Math. classification. 65M08, 76M12, 76M28, 86-08, 76M25, 35L65.

Keywords. Two-phase dusty gas flow model, three-dimensional axial symmetry, compressible Euler equations, pressureless gas dynamics, finite-volume-particle methods, central-upwind schemes, sticky particle methods, operator splitting methods.

1. Introduction

Dusty gases contain a large number of small solid particles (or liquid droplets). The dust phase always has a small volume fraction, but its mass per unit volume may be large relative to the gas phase. Such models are used to describe, for instance, jets of ash in volcanic eruptions (see, e.g., [16, 18, 19, 41, 57, 59]) and arise in many applications ranging from industrial processes to geophysical flows.

The first author was supported by in part by NSF Grants DMS-1115682 and DMS-1521051. The authors also acknowledge the support by NSF RNMS Grant DMS-1107444.
The second author was supported by in part by NSF Grant DMS-1115718.
The third author was supported in part by NSF Grants DMS-1115718 and DMS-1521009.

Dusty gas flows are represented by two-phase models: The first phase (gas), modeled by the compressible Euler equations of gas dynamics, is coupled with the pressureless gas dynamic equations for the second phase (dust) via the drag and heat transfer terms. The model is described by two sets of equations expressed in terms of the density, momentum and total energy of each phase. In this paper, we consider two different dusty gas flow models. The first one is a simplified one-dimensional (1-D) model described in §2.1, while the second one is a more realistic three-dimensional (3-D) model with axial symmetry described in §2.2.

Several numerical methods for dusty gas flow models can be found in, for example, [6, 25, 26, 27, 40, 45, 50, 51]. However, efficiency, accuracy and resolution of these methods are limited due to strong singularities typically developed in the pressureless dusty fraction. In the absence of coupling terms, the studied two-phase systems decouple into two sets of hyperbolic conservation laws. The second (dust) system is a system of pressureless gas dynamics, which may develop δ-shocks either at isolated points or along the surfaces of co-dimension one (see, e.g., [2, 3, 5, 8, 20, 43, 44, 48, 49, 62]). Therefore, numerically solving pressureless gas dynamics equations is a challenging task; see, e.g., [4, 35]. While the source terms present on the right-hand side (RHS) of the studied two-phase systems smooth out singularities in the solution, sharp structures may still develop. Moreover, since the speed of sound of the dusty gas is lower than the speed of sound of the pure gas phase (in fact, substantially lower at high dust densities), the slower dust phase waves are hard to capture using a Riemann-problem-solver-free numerical method (e.g., Godunov-type non-oscillatory central schemes or relaxation schemes) directly applied to the entire two-phase system. On the other hand, developing highly accurate (approximate) Riemann or generalized Riemann problem solvers for the studied systems may be way too complicated and the resulting upwind method may become computationally expensive.

In this paper, we follow the approach in [45, 50] and implement an operator splitting method, in which we split the original two-phase systems into the following three parts: the uncoupled equations for each phase, drag effects and heat transfer systems. We develop new hybrid finite-volume-particle (FVP) methods for the 1-D and axisymmetric 3-D two-phase dusty gas systems by applying a finite-volume (FV) method to the gas component of the system and a sticky particle (SP) method to its dust part.

Any accurate and stable FV method can be used as a part of our hybrid approach. Here, we implement a second-order semi-discrete central-upwind (CU) scheme, which is a Riemann-problem-solver-free Godunov-type method. CU schemes were developed in [29, 30, 32, 33] for general multidimensional hyperbolic systems of conservation laws, and, in particular, were successfully applied to Euler equations of gas dynamics. CU schemes enjoy all the major advantages of Riemann-problem-solver-free central schemes (universality, efficiency and robustness), and at the same time, have a certain "built-in" upwind nature. They can be relatively easily extended to solve the studied two-phase systems, but, as we demonstrate in §5, the resolution of the computed numerical solution may not be sufficiently sharp.

SP methods belong to a class of Lagrangian-type deterministic particle methods (see, e.g., [11, 12, 13, 14, 15, 47]) that provide a diffusion-free (or a low diffusion) alternative to Eulerian FV methods in many cases, especially when a convective term in the underlying system is linear. In these methods, the solution is represented by a collection of particles carrying certain weights. Equations of evolution in time are then written to describe the dynamics of the locations of the particles and their weights. It is well-known that the success of various particle methods relies upon accurate reconstruction procedures used to recover the numerical solution from its particle distribution, as well as on accurate and efficient redistribution algorithms, which will ensure that different regions in the computational domain are adequately resolved. Here, we use a method that is based on the SP method proposed in [14], where a special way of reconstructing the particle velocities as well as a special particle merger technique were developed in order to enforce a desired interaction between the particles and prevent the clustering of particles at the singularities.

In order to design a hybrid approach, we apply the semi-discrete CU scheme to the compressible Euler equations that describe the gas phase and an improved version of the SP method for pressureless gas dynamics equations that represent the dust part. The two methods are combined into the FVP method, which utilizes the specific advantages of each part of the hybrid FVP method in the right places: The high-resolution CU scheme allows one to accurately capture shock, contact and rarefaction waves in the gas fraction, while the low or even non-dissipative SP method guarantees a superb resolution of strong singularities that may form in the dust fraction.

It should be observed that while the CU scheme uses fixed grid cells, the SP method is meshless and particle locations change in time. Therefore, during the interactions steps for the drag effect and heat transfer, the computed cell averages of the gas quantities must be projected onto the particle locations, and the particle approximations of the dust quantities should be averaged over the FV cells. These intergrid projections will be carefully carried out in a sufficiently accurate and conservative manner.

The paper is organized as follows. We start in §2 by describing the studied dusty gas flow models. We then present the 1-D (§3) and axisymmetric 3-D (§4) hybrid FVP methods. We conclude in §5 with several 1-D and axisymmetric 3-D numerical examples and compare solutions computed by the hybrid FVP method with the corresponding solutions computed using the second-order semi-discrete CU scheme applied to the entire system. Our numerical experiments clearly demonstrate the superiority of results obtained by the FVP method.

2. Dusty Gas Flow Models

In this section, we provide a detailed description of the studied 1-D and 3-D dusty gas flow models.

2.1. One-Dimensional Dusty Gas Flow Model

The studied 1-D models reads as

$$\begin{cases} \dfrac{\partial}{\partial t}\boldsymbol{q}_{\rm g} + \dfrac{\partial}{\partial x}\boldsymbol{f}_{\rm g}(\boldsymbol{q}_{\rm g}) = -\boldsymbol{S}_1 - \boldsymbol{S}_2, \\ \dfrac{\partial}{\partial t}\boldsymbol{q}_{\rm d} + \dfrac{\partial}{\partial x}\boldsymbol{f}_{\rm d}(\boldsymbol{q}_{\rm d}) = \boldsymbol{S}_1 + \boldsymbol{S}_2, \end{cases} \tag{2.1}$$

where the subscripts "g" and "d" refer to the gas and dust fractions, respectively,

$$\boldsymbol{q} := \begin{pmatrix} \boldsymbol{q}_{\rm g} \\ \boldsymbol{q}_{\rm d} \end{pmatrix}, \qquad \boldsymbol{q}_{\rm g} = \begin{bmatrix} \rho_{\rm g} \\ \rho_{\rm g} u_{\rm g} \\ E_{\rm g} \end{bmatrix}, \qquad \boldsymbol{q}_{\rm d} = \begin{bmatrix} \rho_{\rm d} \\ \rho_{\rm d} u_{\rm d} \\ E_{\rm d} \end{bmatrix} \tag{2.2}$$

are vectors of conservative variables for gas and dust phases, and

$$\boldsymbol{f}_{\rm g}(\boldsymbol{q}_{\rm g}) = \begin{bmatrix} \rho_{\rm g} u_{\rm g} \\ \rho_{\rm g} u_{\rm g}^2 + p_{\rm g} \\ (E_{\rm g} + p_{\rm g}) u_{\rm g} \end{bmatrix}, \qquad \boldsymbol{f}_{\rm d}(\boldsymbol{q}_{\rm d}) = \begin{bmatrix} \rho_{\rm d} u_{\rm d} \\ \rho_{\rm d} u_{\rm d}^2 \\ E_{\rm d} u_{\rm d} \end{bmatrix} \tag{2.3}$$

are the flux functions for the corresponding phases.

In the above equations (2.1)–(2.3), x and t are space and time variables, respectively, $\rho(x,t)$ is the density, $u(x,t)$ denotes the velocity, $E(x,t)$ is the total energy, $p(x,t)$ represents the pressure. We consider the 1-D model from [45, 50], where the interactions between the two phases due to the drag effect and heat transfer are modeled by the terms $\boldsymbol{S}_1$ and $\boldsymbol{S}_2$ on the RHS of (2.1), which are given by

$$\boldsymbol{S}_1 = \begin{bmatrix} 0 \\ A|u_{\rm g} - u_{\rm d}|(u_{\rm g} - u_{\rm d}) \\ A|u_{\rm g} - u_{\rm d}|(u_{\rm g} - u_{\rm d}) u_{\rm d} \end{bmatrix}, \qquad \boldsymbol{S}_2 = \begin{bmatrix} 0 \\ 0 \\ Q(T_{\rm g} - T_{\rm d}) \end{bmatrix}, \tag{2.4}$$

where $T_{\rm g}$ and $T_{\rm d}$ denote the gas and dust temperatures, respectively. The total energies of the two phases consist of two parts, internal energies ($\mathcal{E}_{\rm g}$ and $\mathcal{E}_{\rm d}$) and kinetic energies ($\mathcal{K}_{\rm g}$ and $\mathcal{K}_{\rm d}$):

$$\begin{aligned} E_{\rm g} &= \mathcal{E}_{\rm g} + \mathcal{K}_{\rm g}, \qquad \mathcal{E}_{\rm g} = \frac{\rho_{\rm g} T_{\rm g}}{\gamma - 1}, \qquad \mathcal{K}_{\rm g} = \frac{1}{2}\rho_{\rm g} u_{\rm g}^2, \\ E_{\rm d} &= \mathcal{E}_{\rm d} + \mathcal{K}_{\rm d}, \qquad \mathcal{E}_{\rm d} = \frac{\rho_{\rm d} T_{\rm d}}{\gamma - 1}, \qquad \mathcal{K}_{\rm d} = \frac{1}{2}\rho_{\rm d} u_{\rm d}^2, \end{aligned} \tag{2.5}$$

where γ stands for the specific heat ratio. The gas pressure $p_{\rm g}$ is computed according to the equation of state (EOS) for an ideal gas,

$$p_{\rm g} = (\gamma - 1)\mathcal{E}_{\rm g}. \tag{2.6}$$

In the interaction terms $\boldsymbol{S}_1$ and $\boldsymbol{S}_2$ in (2.4), A is the drag coefficient and Q is the heat transfer function defined by

$$A = C_{\rm d}\,\rho_{\rm d}\,\rho_{\rm g}, \quad Q = \frac{9\,Nu\,\mu\,\gamma\,\rho_{\rm d}}{2\,u_{\rm ref}\,\rho_{\rm ref}\,d_{\rm p}\,(\gamma-1)\,Pr}, \tag{2.7}$$

where $d_{\rm p}$ is the diameter of the dust particle and the parameters Nu and $C_{\rm d}$ are computed by

$$C_{\rm d} = 0.46 + 28Re^{-0.85} \quad \text{and} \quad Nu = 2 + 0.65Re^{1/2}Pr^{1/3}, \tag{2.8}$$

where Pr denotes the Prandtl number, and Re and μ, which stand for the Reynolds number and dynamic viscosity, respectively, are obtained by

$$Re = \frac{\rho_{\rm g} d_{\rm p}|u_{\rm g} - u_{\rm d}|}{\mu}, \qquad \mu = 1.71 \times 10^{-5}\left(\frac{T_{\rm g}\,T_{\rm ref}}{273}\right)^{0.77}. \tag{2.9}$$

Finally, $\rho_{\rm ref}, u_{\rm ref}$ and $T_{\rm ref}$ are the reference density, viscosity and temperature, respectively.

2.2. **Three-Dimensional Dusty Gas Flow Model with Axial Symmetry**

In the 3-D case with axial symmetry, we denote the fluid density by $\rho(r,z,t)$, its velocities in the r- and z-directions by $u(r,z,t)$ and $v(r,z,t)$, respectively, the total energy by $E(r,z,t)$ and the pressure by $p(r,z,t)$. Using cylindrical coordinates, the axisymmetric 3-D systems of governing equations can be expressed in the following form:

$$\begin{cases} \dfrac{\partial}{\partial t}\boldsymbol{q}_{\rm g} + \dfrac{\partial}{\partial r}\boldsymbol{f}_{\rm g}(\boldsymbol{q}_{\rm g}) + \dfrac{\partial}{\partial z}\boldsymbol{g}_{\rm g}(\boldsymbol{q}_{\rm g}) = \boldsymbol{G}_{\rm g} - \boldsymbol{S}_1 - \boldsymbol{S}_2 + \boldsymbol{S}_r, \\ \dfrac{\partial}{\partial t}\boldsymbol{q}_{\rm d} + \dfrac{\partial}{\partial r}\boldsymbol{f}_{\rm d}(\boldsymbol{q}_{\rm d}) + \dfrac{\partial}{\partial z}\boldsymbol{g}_{\rm d}(\boldsymbol{q}_{\rm d}) = \boldsymbol{G}_{\rm d} + \boldsymbol{S}_1 + \boldsymbol{S}_2, \end{cases} \tag{2.10}$$

where

$$\boldsymbol{q} := \begin{pmatrix} \boldsymbol{q}_{\rm g} \\ \boldsymbol{q}_{\rm d} \end{pmatrix}, \qquad \boldsymbol{q}_{\rm g} = \begin{bmatrix} r\rho_{\rm g} \\ r\rho_{\rm g}u_{\rm g} \\ r\rho_{\rm g}v_{\rm g} \\ rE_{\rm g} \end{bmatrix}, \qquad \boldsymbol{q}_{\rm d} = \begin{bmatrix} r\rho_{\rm d} \\ r\rho_{\rm d}u_{\rm d} \\ r\rho_{\rm d}v_{\rm d} \\ rE_{\rm d} \end{bmatrix}$$

are vectors of conservative variables for gas and dust phases, and

$$\boldsymbol{f}_{\rm g}(\boldsymbol{q}_{\rm g}) = \begin{bmatrix} r\rho_{\rm g}u_{\rm g} \\ r(\rho_{\rm g}u_{\rm g}^2 + p_{\rm g}) \\ r\rho_{\rm g}u_{\rm g}v_{\rm g} \\ ru_{\rm g}(E_{\rm g} + p_{\rm g}) \end{bmatrix}, \quad \boldsymbol{f}_{\rm d}(\boldsymbol{q}_{\rm d}) = \begin{bmatrix} r\rho_{\rm d}u_{\rm d} \\ r\rho_{\rm d}u_{\rm d}^2 \\ r\rho_{\rm d}u_{\rm d}v_{\rm d} \\ rE_{\rm d}u_{\rm d} \end{bmatrix},$$

$$\boldsymbol{g}_{\rm g}(\boldsymbol{q}_{\rm g}) = \begin{bmatrix} r\rho_{\rm g}v_{\rm g} \\ r\rho_{\rm g}u_{\rm g}v_{\rm g} \\ r(\rho_{\rm g}v_{\rm g}^2 + p_{\rm g}) \\ rv_{\rm g}(E_{\rm g} + p_{\rm g}) \end{bmatrix}, \quad \boldsymbol{g}_{\rm d}(\boldsymbol{q}_{\rm d}) = \begin{bmatrix} r\rho_{\rm d}v_{\rm d} \\ r\rho_{\rm d}u_{\rm d}v_{\rm d} \\ r\rho_{\rm d}v_{\rm d}^2 \\ rE_{\rm d}v_{\rm d} \end{bmatrix}$$

are the flux functions for the corresponding phases.

As in the 1-D case, we consider the model from [45, 50], where the interactions between the two phases due to the drag effect and heat transfer are modeled by the terms $\boldsymbol{S}_1$ and $\boldsymbol{S}_2$, respectively, given by

$$\boldsymbol{S}_1 = \begin{bmatrix} 0 \\ rA|\boldsymbol{\mathcal{V}}_{\rm g} - \boldsymbol{\mathcal{V}}_{\rm d}|(u_{\rm g} - u_{\rm d}) \\ rA|\boldsymbol{\mathcal{V}}_{\rm g} - \boldsymbol{\mathcal{V}}_{\rm d}|(v_{\rm g} - v_{\rm d}) \\ rA|\boldsymbol{\mathcal{V}}_{\rm g} - \boldsymbol{\mathcal{V}}_{\rm d}|(\boldsymbol{\mathcal{V}}_{\rm g} - \boldsymbol{\mathcal{V}}_{\rm d})\cdot\boldsymbol{\mathcal{V}}_{\rm d} \end{bmatrix}, \qquad \boldsymbol{S}_2 = \begin{bmatrix} 0 \\ 0 \\ 0 \\ rQ(T_{\rm g} - T_{\rm d}) \end{bmatrix}, \tag{2.11}$$

where $T_{\rm g}$ and $T_{\rm d}$ denote the gas and dust temperatures, while $\boldsymbol{\mathcal{V}}_{\rm g}$ and $\boldsymbol{\mathcal{V}}_{\rm d}$ are their velocity vectors. As in the 1-D case, the total energies of the two phases consist of the internal and kinetic energies and are given by

$$E_{\rm g} = \mathcal{E}_{\rm g} + \mathcal{K}_{\rm g}, \qquad \mathcal{E}_{\rm g} = \frac{\rho_{\rm g} T_{\rm g}}{\gamma - 1}, \qquad \mathcal{K}_{\rm g} = \frac{1}{2}\rho_{\rm g}(u_{\rm g}^2 + v_{\rm g}^2),$$
$$E_{\rm d} = \mathcal{E}_{\rm d} + \mathcal{K}_{\rm d}, \qquad \mathcal{E}_{\rm d} = \frac{\rho_{\rm d} T_{\rm d}\, c_{\rm vd}}{R}, \qquad \mathcal{K}_{\rm d} = \frac{1}{2}\rho_{\rm d}(u_{\rm d}^2 + v_{\rm d}^2),$$

where $c_{\rm vd}$ is the dust specific heat, R is the gas constant, and the gas pressure $p_{\rm g}$ is computed according to the EOS (2.6). In the interaction terms $\boldsymbol{S}_1$ and $\boldsymbol{S}_2$ in (2.11), A is the drag coefficient and Q is the heat transfer function defined by

$$A = C_{\rm d}\,\rho_{\rm d}\,\rho_{\rm g}, \qquad Q = \frac{9\,Nu\,\kappa_{\rm g}\,\rho_{\rm d}\,T_{\rm ref}}{2\,u_{\rm ref}\,p_{\rm ref}\,d_{\rm p}}, \tag{2.12}$$

where $d_{\rm p}$ is the diameter of the dust particle, $\kappa_{\rm g}$ represents the gas thermal conductivity, and the parameters Nu and $C_{\rm d}$ are computed by

$$Nu = 2 + 0.65 Re^{1/2} Pr^{1/3} \quad \text{and} \quad C_{\rm d} = \begin{cases} \frac{24}{Re}(1 + 0.15 Re^{0.687}) & Re < 1000, \\ 0.44 & Re \geq 1000. \end{cases} \tag{2.13}$$

Here, the Reynolds number Re and the Prandtl number Pr are obtained by

$$Re = \frac{\rho_{\rm g} d_{\rm p} |\boldsymbol{\mathcal{V}}_{\rm g} - \boldsymbol{\mathcal{V}}_{\rm d}|}{\mu} \quad \text{and} \quad Pr = \frac{\gamma\, R\, \mu}{(\gamma - 1)\,\kappa_{\rm g}}, \tag{2.14}$$

where μ denotes the dynamic viscosity.

Unlike the 1-D case considered in §2.2, in the axisymmetric 3-D case we have additional geometric and gravitational source terms on the RHS of (2.10) given by

$$\boldsymbol{S}_r = \begin{bmatrix} 0 \\ p_{\rm g} \\ 0 \\ 0 \end{bmatrix}, \qquad \boldsymbol{G}_{\rm g} = \begin{bmatrix} 0 \\ 0 \\ -r\mathfrak{g}\rho_{\rm g} \\ -r\mathfrak{g}\rho_{\rm g} v_{\rm g} \end{bmatrix}, \qquad \boldsymbol{G}_{\rm d} = \begin{bmatrix} 0 \\ 0 \\ -r\mathfrak{g}\rho_{\rm d} \\ -r\mathfrak{g}\rho_{\rm d} v_{\rm d} \end{bmatrix}, \tag{2.15}$$

where the parameter $\mathfrak{g}$ denotes the gravitational constant.

The presence of the extra terms (2.15) brings another level of complexity to the construction of an accurate numerical method for (2.10) as the system admits steady-state solutions with the hydrostatic balance if the dust phase is omitted. At these "dust-free" steady states, the flux produced by the pressure in the gas phase is canceled by the gravitational source term and the resulting steady-state solution is

$$u_{\rm g} \equiv 0, \quad v_{\rm g} \equiv 0, \quad p_{\rm g} = p_{\rm g}(z), \quad w_{\rm g} := p_{\rm g} + R_{\rm g} \equiv \text{Const}, \tag{2.16}$$

where $R_{\rm g}$ is the primitive of the gravitational force in the vertical direction, that is,

$$R_{\rm g}(r, z, t) := \mathfrak{g} \int^{z} \rho_{\rm g}(r, \zeta, t) d\zeta. \tag{2.17}$$

The importance of steady states such as (2.16) lies in the fact that in many situations when the dust phase is absent, the dynamics is realized as a (relatively) small perturbation of the steady states. It is therefore essential to design a well-balanced numerical method, that is, a numerical method, which preserves a discrete version of the equilibrium states (2.16) exactly. An improper treatment of the gravitational force and thus the steady states may lead to a solution, which either oscillates around the equilibrium or deviates from the equilibrium in time. This problem is well known in the numerical community and received a great attention in the literature; see, e.g., [1, 7, 9, 17, 36, 37, 39, 55, 56, 60, 61].

For the compressible Euler equations that describe the gas phase, we use a well-balanced version of the second-order semi-discrete CU scheme introduced in [9]. We follow the idea in [9] and perform the piecewise linear reconstruction step of the CU scheme in such a way that the equilibrium variables remain constants at the steady states. The latter is achieved by reconstructing the equilibrium variables rather than the conservative ones and results in a well-balanced CU scheme for the Euler equations governing the gas phase; see §4.1.1 below.

3. One-Dimensional Finite-Volume-Particle (FVP) Method

We develop a numerical method for the dusty gas system (2.1) using an operator splitting approach. We split the system (2.1) into three parts. The first part is the homogeneous equations of the gas and dust phases:

$$\begin{cases} \dfrac{\partial}{\partial t}\boldsymbol{q}_{\mathrm{g}} + \dfrac{\partial}{\partial x}\boldsymbol{f}_{\mathrm{g}}(\boldsymbol{q}_{\mathrm{g}}) = 0, & (3.1a)\\ \dfrac{\partial}{\partial t}\boldsymbol{q}_{\mathrm{d}} + \dfrac{\partial}{\partial x}\boldsymbol{f}_{\mathrm{d}}(\boldsymbol{q}_{\mathrm{d}}) = 0, & (3.1b)\end{cases}$$

the second part represents the drag effect between the two phases:

$$\begin{cases} \dfrac{\partial}{\partial t}\boldsymbol{q}_{\mathrm{g}} = -\boldsymbol{S}_1, & (3.2a)\\ \dfrac{\partial}{\partial t}\boldsymbol{q}_{\mathrm{d}} = \boldsymbol{S}_1, & (3.2b)\end{cases}$$

and lastly, the third part stands for the heat transfer:

$$\begin{cases} \dfrac{\partial}{\partial t}\boldsymbol{q}_{\mathrm{g}} = -\boldsymbol{S}_2, & (3.3a)\\ \dfrac{\partial}{\partial t}\boldsymbol{q}_{\mathrm{d}} = \boldsymbol{S}_2. & (3.3b)\end{cases}$$

We denote the solution operators for (3.1), (3.2), (3.3) by $\mathcal{L}_0$, $\mathcal{L}_1$ and $\mathcal{L}_2$, respectively, and assume that the solution at time t is available. Then, the solution at time $t+\Delta t$ is approximated using the second-order Strang splitting [53]:

$$\boldsymbol{q}(x,t+\Delta t) \approx \mathcal{L}_0\Big(\frac{\Delta t}{2}\Big)\mathcal{L}_1\Big(\frac{\Delta t}{2}\Big)\mathcal{L}_2(\Delta t)\mathcal{L}_1\Big(\frac{\Delta t}{2}\Big)\mathcal{L}_0\Big(\frac{\Delta t}{2}\Big)\boldsymbol{q}(x,t). \tag{3.4}$$

Note that the first part (3.1) consists of two uncoupled systems (3.1a) and (3.1b), which can be solved separately, while the coupling between the gas and dust phases is reflected in the systems (3.2) and (3.3).

In the following sections, we introduce the numerical schemes for the fluid dynamics (3.1a), (3.1b), drag effects (3.2) and heat transfer (3.3) splitting steps.

3.1. $\mathcal{L}_0$: Fluid Dynamics Splitting Step

In this section, we introduce an FVP method for the uncoupled systems (3.1). In this method, the gas phase system (3.1a) is solved by a CU scheme while the dust phase system (3.1b) is solved by an SP method.

3.1.1. *Semi-Discrete Central-Upwind (CU) Scheme for the Gas Phase*

We start with a description of a semi-discrete CU scheme for the system (3.1a). For simplicity, we partition the computational domain into uniform cells $C_j := [x_{j-\frac{1}{2}}, x_{j+\frac{1}{2}}]$ of size $|C_j| = \Delta x$ centered at $x_j = j\Delta x,\ \ j = j_L, \ldots, j_R$. We assume that at time level t, the cell averages of the numerical solution, $(\overline{\boldsymbol{q}_{\rm g}})_j(t) := \frac{1}{\Delta x}\int_{C_j} \boldsymbol{q}_{\rm g}(x,t)\,dx$, are available.

A semi-discrete CU scheme from [30] applied to (3.1a) results in the following system of ODEs:

$$\frac{d}{dt}\,(\overline{\boldsymbol{q}_{\rm g}})_j = -\frac{\boldsymbol{\mathcal{F}}_{j+\frac{1}{2}} - \boldsymbol{\mathcal{F}}_{j-\frac{1}{2}}}{\Delta x}, \tag{3.5}$$

where

$$\boldsymbol{\mathcal{F}}_{j+\frac{1}{2}} := \frac{a^+_{j+\frac{1}{2}}\boldsymbol{f}_{\rm g}((\boldsymbol{q}_{\rm g})^{\rm E}_j) - a^-_{j+\frac{1}{2}}\boldsymbol{f}_{\rm g}((\boldsymbol{q}_{\rm g})^{\rm W}_{j+1})}{a^+_{j+\frac{1}{2}} - a^-_{j+\frac{1}{2}}} + \frac{a^+_{j+\frac{1}{2}}a^-_{j+\frac{1}{2}}}{a^+_{j+\frac{1}{2}} - a^-_{j+\frac{1}{2}}}\Big((\boldsymbol{q}_{\rm g})^{\rm W}_{j+1} - (\boldsymbol{q}_{\rm g})^{\rm E}_j\Big) \tag{3.6}$$

are numerical fluxes.

The one-sided point values in (3.6) are computed by

$$(\boldsymbol{q}_{\rm g})^{\rm E}_j := \Big[(\rho_{\rm g})^{\rm E}_j, (\rho_{\rm g})^{\rm E}_j(u_{\rm g})^{\rm E}_j, \frac{(p_{\rm g})^{\rm E}_j}{\gamma-1} + \frac{1}{2}(\rho_{\rm g})^{\rm E}_j((u_{\rm g})^{\rm E}_j)^2\Big]^T,$$

$$(\boldsymbol{q}_{\rm g})^{\rm W}_{j+1} := \Big[(\rho_{\rm g})^{\rm W}_{j+1}, (\rho_{\rm g})^{\rm W}_{j+1}(u_{\rm g})^{\rm W}_{j+1}, \frac{(p_{\rm g})^{\rm W}_{j+1}}{\gamma-1} + \frac{1}{2}(\rho_{\rm g})^{\rm W}_{j+1}((u_{\rm g})^{\rm W}_{j+1})^2\Big]^T,$$

where $(\rho_{\rm g})^{\rm E}_j$, $(u_{\rm g})^{\rm E}_j$, $(p_{\rm g})^{\rm E}_j$ (and $(\rho_{\rm g})^{\rm W}_{j+1}$, $(u_{\rm g})^{\rm W}_{j+1}$, $(p_{\rm g})^{\rm W}_{j+1}$) are the left- (right-) sided values of the gas density, velocity and pressure at the cell interfaces $x = x_{j+\frac{1}{2}}$, which are obtained using the reconstruction operator $\mathcal{R}$ (introduced in Appendix A.1):

$$\begin{aligned}
&(\rho_{\rm g})^{\rm E}_j := \mathcal{R}\{(\overline{\rho_{\rm g}})_j\}\big|_{x=x^-_{j+\frac{1}{2}}}, \quad (u_{\rm g})^{\rm E}_j := \mathcal{R}\{(u_{\rm g})_j\}\big|_{x=x^-_{j+\frac{1}{2}}}, \quad (p_{\rm g})^{\rm E}_j := \mathcal{R}\{(p_{\rm g})_j\}\big|_{x=x^-_{j+\frac{1}{2}}},\\
&(\rho_{\rm g})^{\rm W}_{j+1} := \mathcal{R}\{(\overline{\rho_{\rm g}})_j\}\big|_{x=x^+_{j+\frac{1}{2}}}, \quad (u_{\rm g})^{\rm W}_{j+1} := \mathcal{R}\{(u_{\rm g})_j\}\big|_{x=x^+_{j+\frac{1}{2}}}, \quad (p_{\rm g})^{\rm W}_{j+1} := \mathcal{R}\{(p_{\rm g})_j\}\big|_{x=x^+_{j+\frac{1}{2}}}.
\end{aligned} \tag{3.7}$$

Here,

$$(u_{\rm g})_j = \frac{(\overline{\rho_{\rm g}u_{\rm g}})_j}{(\overline{\rho_{\rm g}})_j} \quad \text{and} \quad (p_{\rm g})_j = (\gamma-1)\Big[(\overline{E_{\rm g}})_j - \frac{1}{2}(\overline{\rho_{\rm g}})_j(u_{\rm g})^2_j\Big] \tag{3.8}$$

are approximations of the cell center values of the gas velocity and pressure, respectively.

Finally, the one-sided local speeds of propagation, $a^\pm_{j+\frac{1}{2}}$, in (3.6) are estimated using the smallest and largest eigenvalues of the Jacobian $\frac{\partial \boldsymbol{f}_{\rm g}}{\partial \boldsymbol{q}_{\rm g}}$:

$$\begin{aligned}
a^+_{j+\frac{1}{2}} &= \max\Big\{(u_{\rm g})^{\rm E}_j + (c_{\rm g})^{\rm E}_j,\ (u_{\rm g})^{\rm W}_{j+1} + (c_{\rm g})^{\rm W}_{j+1},\ 0\Big\},\\
a^-_{j+\frac{1}{2}} &= \min\Big\{(u_{\rm g})^{\rm E}_j - (c_{\rm g})^{\rm E}_j,\ (u_{\rm g})^{\rm W}_{j+1} - (c_{\rm g})^{\rm W}_{j+1},\ 0\Big\},
\end{aligned} \tag{3.9}$$

where the speeds of sound are defined by $(c_{\rm g})^{\rm E}_j := \sqrt{\dfrac{\gamma(p_{\rm g})^{\rm E}_j}{(\rho_{\rm g})^{\rm E}_j}}$ and $(c_{\rm g})^{\rm W}_{j+1} := \sqrt{\dfrac{\gamma(p_{\rm g})^{\rm W}_{j+1}}{(\rho_{\rm g})^{\rm W}_{j+1}}}$.

Remark 3.1. In (3.7), (3.8), we reconstruct the primitive variables $(\rho_{\rm g}, u_{\rm g}, p_{\rm g})$ rather than the conservative ones $(\rho_{\rm g}, \rho_{\rm g}u_{\rm g}, E_{\rm g})$, since our numerical experiments suggest that reconstructing the conservative variables may lead to appearance of oscillations in the velocity and temperature across contact waves.

Remark 3.2. We would like to point out that the first-order version of the scheme (3.5), (3.6) is exactly the semi-discrete version of the scheme in [21, 28].

3.1.2. *Sticky Particle (SP) Method for the Dust Phase*

In this section, we describe the sticky particle method from [14], which is used to solve the dust phase system (3.1b). To this end, we seek a solution of (3.1b) in the form of a linear combination of δ-functions:

$$\boldsymbol{q}_{\rm d}^M(x,t) = \sum_{i=1}^{M} \boldsymbol{\alpha}_i(t)\delta(x - x_i^{\mathcal{P}}(t)), \qquad \boldsymbol{\alpha}_i = (\, m_i, m_i(u_{\rm d})_i, (E_{\rm d})_i\,)^T. \tag{3.10}$$

Here, M denotes a total number of particles, $x_i^{\mathcal{P}}$ and $\boldsymbol{\alpha}_i$ are the location and weights of the $i^{\rm th}$ particle that carries the mass m_i, momentum $m_i(u_{\rm d})_i$ and energy $(E_{\rm d})_i$.

The initial weights and locations of the particles can be determined based on the the initial condition $q_{\rm d}(x,0) = \big(\rho_{\rm d}(x,0), \rho_{\rm d}u_{\rm d}(x,0), E_{\rm d}(x,0)\big)^T$. We first partition the computational domain Ω into M subdomains Ω_i^0, $i = 1,\ldots,M$, and then an $i^{\rm th}$ particle with the weight $\boldsymbol{\alpha}_i(0) := \int_{\Omega_i^0} \boldsymbol{q}_{\rm d}(x,0)dx$ is placed at the geometric center of Ω_i^0, denoted by $x_i^{\mathcal{P}}(0)$. For example, one may choose $\{\Omega_i^0\}$ to be an uniform partition of the computational domain Ω, and $x_i^{\mathcal{P}}(0)$ to be the center of the interval Ω_i^0. Then, the particle weights are approximated by a midpoint quadrature:

$$\boldsymbol{\alpha}_i(0) = \int\limits_{\Omega_i^0} \boldsymbol{q}_{\rm d}(x,0)dx \approx |\Omega_i^0|\boldsymbol{q}_{\rm g}(x_i^{\mathcal{P}}(0),0).$$

Based on the weak formulation of (3.1b) the locations and weights of particles are evolved according to the following ODEs (see [14]):

$$\frac{dx_i^{\mathcal{P}}(t)}{dt} = \widetilde{u_{\rm d}}(x_i^{\mathcal{P}}(t),t), \qquad \frac{d\boldsymbol{\alpha}_i(t)}{dt} = \mathbf{0}, \qquad i = 1,\ldots,M, \tag{3.11}$$

where $\widetilde{u_{\rm d}}(x,t)$ is a piecewise linear reconstruction of the dust velocity obtained in the following way. First, we compute the average velocities of the particles located in each cell C_j. These velocities, denoted by $(u_{\rm d})_j^{\rm CM}$, are computed by

$$(u_{\rm d})_j^{\rm CM} = \frac{\sum\limits_{i:x_i^{\mathcal{P}}(t)\in C_j} \alpha_i^{(2)}(t)}{\sum\limits_{i:x_i^{\mathcal{P}}(t)\in C_j} \alpha_i^{(1)}(t)}$$

and can be viewed as approximate dust velocity values at the corresponding centers of mass:

$$(u_{\rm d})_j^{\rm CM} \approx u_{\rm d}(x_j^{\rm CM},t), \qquad x_j^{\rm CM} = \frac{\sum\limits_{i:x_i^{\mathcal{P}}(t)\in C_j} x_i^{\mathcal{P}}(t)\alpha_i^{(1)}(t)}{\sum\limits_{i:x_i^{\mathcal{P}}(t)\in C_j} \alpha_i^{(1)}(t)}. \tag{3.12}$$

Then, we reconstruct the piecewise linear approximation of $u_{\rm d}$ as follows:

$$\widetilde{u_{\rm d}}(x,t) = \mathcal{R}^{\mathcal{P}}\left\{\big((u_{\rm d})_j^{\rm CM}, x_j^{\rm CM}\big)\right\},$$

where the reconstruction operator $\mathcal{R}^{\mathcal{P}}$ is introduced in Appendix B.1.

For each particle, in addition to evolving its location and weights, we also need to keep track of the volume $|\Omega_i|$ occupied by the particle (it will be used in the computation of the exchange terms, see §3.4). As in [11], we evolve $|\Omega_i(t)|$ by solving the following ODEs:

$$\frac{d}{dt}|\Omega_i(t)| = \frac{\partial \widetilde{u_{\rm d}}}{\partial x}(x_i^{\mathcal{P}}(t),t)|\Omega_i(t)|, \tag{3.13}$$

subject to the initial conditions $|\Omega_i(0)| = |\Omega_i^0|$.

3.1.3. *Particle Merger*

In cases when too many particles cluster in a relatively small region, the efficiency of the particle method is significantly jeopardized. This happens due to severe time step restrictions needed to ensure the stability of the particle method (as it becomes unstable if one allows the particle trajectories to cross in the (x,t)-plane). To overcome this difficulty, we adopt the following particle merger algorithm from [14]: We choose a predetermined critical distance d_{cr} and force any two particles, say, the $i^{\rm th}$ and $i+1^{\rm st}$, with the distance between them smaller than d_{cr} to be merged into a new particle whose the weight and location are calculated as:

$$\boldsymbol{\alpha}^{\rm new} = \boldsymbol{\alpha}_i + \boldsymbol{\alpha}_{i+1}, \qquad x^{\rm new} = \frac{m_i x_i^{\mathcal{P}} + m_{i+1}x_{i+1}^{\mathcal{P}}}{m_i + m_{i+1}}.$$

This procedure of particle merger is repeated until the distance between any pair of remaining particles is greater than d_{cr}.

Remark 3.3. The critical distance d_{cr} should be chosen experimentally. In all of our numerical examples, this distance was set as $d_{cr} = \Delta x/2$. We would also like to stress that our numerical experiments clearly indicate that the presented FVP method does not seem to be sensitive to the choice of d_{cr}.

3.1.4. *Particle Redistribution*

While some particles may cluster, some other particles may spread away from each other, in which cases some of the particles become isolated and, as a result, the particle distribution will become too sparse to provide a sufficient resolution of the computed solution. Therefore, we propose the following procedure to detect and locally redistribute the isolated particles. First, the total number of particles located in C_j is counted and denoted by n_j. If one of the particle-occupied cells ($n_j > 0$) has "empty" neighboring cells (that is, both $n_{j-1} = 0$ and $n_{j+1} = 0$), then we regard the particles in this cell as isolated. We then replace all of the isolated particles in the computational domain with a new group of particles located at the centers of the FV cells $\{x_\ell\}$ and carrying the weights $\{\boldsymbol{\alpha}_\ell^{\rm new}\}$ given by

$$\boldsymbol{\alpha}_\ell^{\rm new} = \sum_{i\in I} \Phi\Big(\frac{x_i^{\mathcal{P}} - x_\ell}{\Delta x}\Big)\boldsymbol{\alpha}_i, \quad I = \{\, i \mid x_i^{\mathcal{P}} \in C_j : n_j > 0,\ n_{j-1} = n_{j+1} = 0\}, \tag{3.14}$$

where

$$\Phi(\xi) = \begin{cases} 5 - 2\xi - \dfrac{1}{8}\sqrt{-7 + 12\xi - 4\xi^2}, & \text{if } 1 < |\xi| \le 2, \\ 3 - 2\xi + \dfrac{1}{8}\sqrt{1 + 4\xi - 4\xi^2}, & \text{if } |\xi| \le 1, \\ 0, & \text{otherwise} \end{cases} \tag{3.15}$$

is a nonnegative compactly supported cut-off function [34, 46]. It can be shown that the redistribution procedure described above satisfies the conservation of mass, momentum and energy of particles:

$$\sum_\ell \boldsymbol{\alpha}_\ell^{\rm new} = \sum_{i\in I} \boldsymbol{\alpha}_i. \tag{3.16}$$

Remark 3.4. Note that in (3.14),

$$\Phi\Big(\frac{x_i^{\mathcal{P}}-x_\ell}{\Delta x}\Big)=0,\quad \text{if}\quad x_i^{\mathcal{P}}-x_\ell\geq 2\Delta x,$$

which indicates that the new particles generated far away from isolated particles will have zero weights and it is sufficient to only consider the new particles located within the $2\Delta x$ vicinity of the isolated particles. In fact, if the particles in a certain cell C_j are detected as isolated, we only compute their replacements $\{x_\ell,\boldsymbol{\alpha}_\ell^{\text{new}}\}$ with $\ell=j-2,\ldots,j+2$.

3.2. $\mathcal{L}_1$: Interaction Time Step for Drag Effect

In this section, we describe the numerical scheme for solving the system (3.2) over the time interval $[t_0,t_0+\Delta t]$ (we follow the approach in [45]). In this procedure, denoted by $\mathcal{L}_1(\Delta t)$, the gas and dust phases exchange a portion of their momentum and energy due to the drag effect. Omitting the dependence on x, we rewrite (3.2) as the following system of ODEs:

$$\frac{d}{dt}\rho_{\text{g}}(t)=0, \tag{3.17a}$$

$$\frac{d}{dt}\rho_{\text{g}}u_{\text{g}}(t)=-A\,|u_{\text{g}}(t)-u_{\text{d}}(t)|\,\big(u_{\text{g}}(t)-u_{\text{d}}(t)\big), \tag{3.17b}$$

$$\frac{d}{dt}E_{\text{g}}(t)=-A\,|u_{\text{g}}(t)-u_{\text{d}}(t)|\,\big(u_{\text{g}}(t)-u_{\text{d}}(t)\big)\,u_{\text{d}}(t), \tag{3.17c}$$

$$\frac{d}{dt}\rho_{\text{d}}(t)=0, \tag{3.17d}$$

$$\frac{d}{dt}\rho_{\text{d}}u_{\text{d}}(t)=A\,|u_{\text{g}}(t)-u_{\text{d}}(t)|\,\big(u_{\text{g}}(t)-u_{\text{d}}(t)\big), \tag{3.17e}$$

$$\frac{d}{dt}E_{\text{d}}(t)=A\,|u_{\text{g}}(t)-u_{\text{d}}(t)|\,\big(u_{\text{g}}(t)-u_{\text{d}}(t)\big)\,u_{\text{d}}(t). \tag{3.17f}$$

We note that ρ_{g} and ρ_{d} remain constant during this splitting step and following [45], we assume that the coefficient A is also constant for $t\in[t_0,t_0+\Delta t]$. Then, equations (3.17b), (3.17c), (3.17e), (3.17f) can be explicitly solved and their solutions are

$$\begin{aligned}(\rho_{\text{g}}u_{\text{g}})(t_0+\Delta t)&=(\rho_{\text{g}}u_{\text{g}})(t_0)+M_1^{\text{ex}},\\(\rho_{\text{d}}u_{\text{d}})(t_0+\Delta t)&=(\rho_{\text{d}}u_{\text{d}})(t_0)-M_1^{\text{ex}},\\E_{\text{g}}(t_0+\Delta t)&=E_{\text{g}}(t_0)+E_1^{\text{ex}},\\E_{\text{d}}(t_0+\Delta t)&=E_{\text{d}}(t_0)-E_1^{\text{ex}},\end{aligned}$$

where

$$M_1^{\text{ex}}=\frac{\Delta u}{\xi}\left(\frac{1}{\tau}-1\right)\quad\text{and}\quad E_1^{\text{ex}}=|\Delta u|^3\frac{A\Delta t\,(1+\tau)}{2\xi\tau^2\rho_{\text{d}}(t_0)}-A\,\widehat{u}\,\Delta u|\Delta u|\frac{\Delta t}{\tau} \tag{3.18}$$

are the momentum and energy exchanges between the two phases. Here,

$$\Delta u=u_{\text{g}}(t_0)-u_{\text{d}}(t_0),\quad \widehat{u}=\frac{\rho_{\text{g}}(t_0)u_{\text{g}}(t_0)+\rho_{\text{d}}(t_0)u_{\text{d}}(t_0)}{\rho_{\text{g}}(t_0)+\rho_{\text{d}}(t_0)}, \tag{3.19}$$

$$\xi=\frac{1}{\rho_{\text{g}}(t_0)}+\frac{1}{\rho_{\text{d}}(t_0)},\quad \tau=1+A\,\xi|\Delta u|\Delta t, \tag{3.20}$$

and the coefficient A is computed using (2.7)–(2.9) at time $t=t_0$.

As described in §3.1.1 and §3.1.2, the numerical solutions of the two phases are evolved in different forms: the solution of the gas phase is realized in terms of cell averages on a fixed grid while the

solution of the dust phase is realized in terms of a meshless particle distribution. Therefore, to evolve the numerical solutions of both phases, the system (3.17) has to be solved twice, at two different sets of locations for two phases.

On one hand, for the gas phase, its average momentum and energy in the cell C_j are evolved using the momentum and energy exchanges M_1^{ex} and E_1^{ex} computed at x_j:

$$(\overline{\rho_{\mathrm{g}} u_{\mathrm{g}}})_j(t_0+\Delta t) = (\overline{\rho_{\mathrm{g}} u_{\mathrm{g}}})_j(t_0) + M_1^{\mathrm{ex}}(x_j), \tag{3.21}$$

$$(\overline{E_{\mathrm{g}}})_j(t_0+\Delta t) = (\overline{E_{\mathrm{g}}})_j(t_0) + E_1^{\mathrm{ex}}(x_j). \tag{3.22}$$

On the other hand, for the dust phase, the momentum and energy weights of the ith particle are evolved using the exchange terms calculated at $x_i^{\mathcal{P}}$:

$$\alpha^{(2)}(t_0+\Delta t) = \alpha^{(2)}(t_0) + |\Omega_i| M_1^{\mathrm{ex}}(x_i^{\mathcal{P}}), \tag{3.23}$$

$$\alpha^{(3)}(t_0+\Delta t) = \alpha^{(3)}(t_0) + |\Omega_i| E_1^{\mathrm{ex}}(x_i^{\mathcal{P}}). \tag{3.24}$$

In (3.21)–(3.24), the exchange terms are explicitly computed using the formulas (3.18)–(3.20), where the temperature value of the gas phase as well as the density and velocity values of the two phases at locations $x = x_j$ and $x = x_i^{\mathcal{P}}$ are needed. To this end, we need to project the FV data onto the particle locations $\{x_i^{\mathcal{P}}\}$, and the particle data onto the cell centers $\{x_j\}$. These projections are introduced in §3.4.

3.3. $\mathcal{L}_2$: Interaction Time Step for Heat Transfer

In this section, we review the numerical scheme proposed in [45] for solving the system (3.3) over the time interval $[t_0, t_0+\Delta t]$. In this procedure, denoted by $\mathcal{L}_2$, the gas and dust phases exchange a portion of their internal energies due to their temperature difference and the heat transfer between them. Again, we omit the dependence on x and rewrite (3.3) as the following system of ODEs:

$$\frac{d}{dt}\rho_{\mathrm{g}}(t) = 0, \tag{3.25a}$$

$$\frac{d}{dt}\rho_{\mathrm{g}} u_{\mathrm{g}}(t) = 0, \tag{3.25b}$$

$$\frac{d}{dt}E_{\mathrm{g}}(t) = -Q\,(T_{\mathrm{g}}(t) - T_{\mathrm{d}}(t)), \tag{3.25c}$$

$$\frac{d}{dt}\rho_{\mathrm{d}}(t) = 0, \tag{3.25d}$$

$$\frac{d}{dt}\rho_{\mathrm{d}} u_{\mathrm{d}}(t) = 0, \tag{3.25e}$$

$$\frac{d}{dt}E_{\mathrm{d}}(t) = Q\,(T_{\mathrm{g}}(t) - T_{\mathrm{d}}(t)). \tag{3.25f}$$

Noting that the densities and momenta of both phases remain constant during this splitting step, we assume that the coefficient Q is constant for $t \in [t_0, t_0+\Delta t]$. As the result, the kinetic energies remain unchanged and only the internal energies $\mathcal{E}_{\mathrm{g}}$ and $\mathcal{E}_{\mathrm{d}}$ are evolved by (3.25). According to the relations between the temperature and internal energy (as introduced in (2.5)), we rewrite the ODEs (3.25c) and (3.25f) as

$$\frac{d}{dt}T_{\mathrm{g}}(t) = -\frac{Q(\gamma-1)}{\rho_{\mathrm{g}}}\,(T_{\mathrm{g}}(t) - T_{\mathrm{d}}(t)),$$

$$\frac{d}{dt}T_{\mathrm{d}}(t) = \frac{Q(\gamma-1)}{\rho_{\mathrm{d}}}\,(T_{\mathrm{g}}(t) - T_{\mathrm{d}}(t)).$$

These equations can be analytically solved, and their solutions can be used to evolve $E_{\rm g}$ and $E_{\rm d}$ as follows:

$$E_{\rm g}(t_0+\Delta t) = E_{\rm g}(t_0) + E_2^{\rm ex},$$
$$E_{\rm d}(t_0+\Delta t) = E_{\rm d}(t_0) - E_2^{\rm ex},$$

where

$$E_2^{\rm ex} = \frac{T_{\rm g}(t_0) - T_{\rm d}(t_0)}{\eta}\left[e^{-Q\,\eta\,\Delta t} - 1\right] \tag{3.26}$$

is the energy exchange between the two phases. Here,

$$\eta = (\gamma-1)\left[\frac{1}{\rho_{\rm g}} + \frac{1}{\rho_{\rm d}}\right], \tag{3.27}$$

and the coefficient Q is computed using (2.7)–(2.9) at time $t = t_0$.

Once again, in order to evolve the numerical solutions of the two phases, the ODE system (3.25) has to be solved at two sets of locations. For the gas phase, the average energy in C_j is updated by

$$(\overline{E_{\rm g}})_j(t_0+\Delta t) = (\overline{E_{\rm g}})_j(t_0) + E_2^{\rm ex}(x_j),$$

and for the dust phase, the energy weight of the $i^{\rm th}$ particle is evolved by

$$\alpha_i^{(3)}(t_0+\Delta t) = \alpha_i^{(3)}(t_0) + |\Omega_i(t_0)|E_2^{\rm ex}(x_i^{\mathcal{P}}).$$

Here, the energy exchanges $E_2^{\rm ex}(x_j)$ and $E_2^{\rm ex}(x_i^{\mathcal{P}})$ are computed at both $x = x_j$ and $x = x_i^{\mathcal{P}}$ using the formulas (3.26) and (3.27), in which the density, velocity and temperature values of the two phases are required. In the next section, we will introduce how to obtain those values by projecting the FV data onto the particle locations and the particle data onto the cell centers.

Remark 3.5. Since in the interaction time steps $\mathcal{L}_1$ and $\mathcal{L}_2$, only the momenta and energies of the two phases are locally exchanged and the transportation of neither phase is considered, therefore, both the locations of particles $\{x_i^{\mathcal{P}}(t)\}$ and the corresponding occupied volumes $\{|\Omega_i(t)|\}$ remain unchanged during these two splitting steps, see (3.11) and (3.13).

3.4. **Finite-Volume and Particle Data Projection**

Here, we describe the numerical techniques used to project the FV data onto the set of particle locations $\{x_i^{\mathcal{P}}(t)\}$ and the particle data onto the cell centers $\{x_j\}$. We assume that the gas- and dust-phase numerical solutions, namely, $\{(\overline{\boldsymbol{q}_{\rm g}})_j(t)\}$ and $\{\boldsymbol{\alpha}_i(t), x_i^{\mathcal{P}}(t)\}$, are available at a certain time level t.

First, to evaluate the dust data at the cell centers, we use the piecewise linear reconstruction operator $\mathcal{R}^{\mathcal{P}}$ to obtain (see Appendix B.1):

$$\rho_{\rm d}(x_j,t) = \mathcal{R}^{\mathcal{P}}\left\{\left(\frac{1}{\Delta x}\sum_{i:x_i^{\mathcal{P}}\in C_j}\alpha_i^{(1)}(t), x_j^{\rm CM}\right)\right\}\Bigg|_{x=x_j},$$

$$u_{\rm d}(x_j,t) = \mathcal{R}^{\mathcal{P}}\left\{\left(\frac{\sum\limits_{i:x_i^{\mathcal{P}}\in C_j}\alpha_i^{(2)}(t)}{\sum\limits_{i:x_i^{\mathcal{P}}\in C_j}\alpha_i^{(1)}(t)}, x_j^{\rm CM}\right)\right\}\Bigg|_{x=x_j},$$

$$T_{\rm d}(x_j,t) = \mathcal{R}^{\mathcal{P}}\left\{\left(\frac{1}{c_{\rm vd}}\left[\frac{\sum\limits_{i:x_i^{\mathcal{P}}\in C_j}\alpha_i^{(3)}(t)}{\sum\limits_{i:x_i^{\mathcal{P}}\in C_j}\alpha_i^{(1)}(t)} - \frac{1}{2}\left(\frac{\sum\limits_{i:x_i^{\mathcal{P}}\in C_j}\alpha_i^{(2)}(t)}{\sum\limits_{i:x_i^{\mathcal{P}}\in C_j}\alpha_i^{(1)}(t)}\right)^2\right], x_j^{\rm CM}\right)\right\}\Bigg|_{x=x_j},$$

where x_j^{CM} are the centers of mass of the particles located in the cell C_j, see (3.12).

Using the reconstruction operator $\mathcal{R}$ (see Appendix A.1), we then project the gas data onto the set of particle locations:

$$\rho_{\mathrm{g}}(x_i^{\mathcal{P}}(t),t)=\mathcal{R}\left\{(\overline{\rho_{\mathrm{g}}})_j(t)\right\}\big|_{x=x_i^{\mathcal{P}}(t)},\ u_{\mathrm{g}}(x_i^{\mathcal{P}}(t),t)=\mathcal{R}\left\{(u_{\mathrm{g}})_j(t)\right\}\big|_{x=x_i^{\mathcal{P}}(t)},$$

$$T_{\mathrm{g}}(x_i^{\mathcal{P}}(t),t)=\mathcal{R}\left\{(T_{\mathrm{g}})_j(t)\right\}\big|_{x=x_i^{\mathcal{P}}(t)},$$

where

$$(u_{\mathrm{g}})_j(t)=\frac{(\overline{\rho_{\mathrm{g}}u_{\mathrm{g}}})_j(t)}{(\overline{\rho_{\mathrm{g}}})_j(t)}\quad\text{and}\quad(T_{\mathrm{g}})_j(t)=(\gamma-1)\left[\frac{(\overline{E_{\mathrm{g}}})_j(t)}{(\overline{\rho_{\mathrm{g}}})_j(t)}-\frac{1}{2}(u_{\mathrm{g}})_j^2(t)\right].$$

Finally, the point values of the dust phase are directly computed using the particle weights and the size of the domain occupied by the particle:

$$\rho_{\mathrm{d}}(x_i^{\mathcal{P}}(t),t)=\frac{\alpha_i^{(1)}(t)}{|\Omega_i(t)|},\quad u_{\mathrm{d}}(x_i^{\mathcal{P}}(t),t)=\frac{\alpha_i^{(2)}(t)}{\alpha_i^{(1)}(t)},\quad T_{\mathrm{d}}(x_i^{\mathcal{P}}(t),t)=(\gamma-1)\left[\frac{\alpha_i^{(3)}(t)}{\alpha_i^{(1)}(t)}-\frac{1}{2}u_{\mathrm{d}}^2(x_i^{\mathcal{P}}(t),t)\right].$$

4. Axisymmetric Three-Dimensional Finite-Volume-Particle (FVP) Method

In this section, we develop a numerical method for the axisymmetric 3-D dusty gas system (2.10). As in the 1-D case, our method is based on an operator splitting approach according to which the system (2.10) is split into three parts. The first part consists of the conservation equations for both phases and the geometric and gravitational source terms:

$$\begin{cases}\dfrac{\partial}{\partial t}\boldsymbol{q}_{\mathrm{g}}+\dfrac{\partial}{\partial r}\boldsymbol{f}_{\mathrm{g}}(\boldsymbol{q}_{\mathrm{g}})+\dfrac{\partial}{\partial z}\boldsymbol{g}_{\mathrm{g}}(\boldsymbol{q}_{\mathrm{g}})=\boldsymbol{G}_{\mathrm{g}}+\boldsymbol{S}_r, & (4.1\mathrm{a})\\ \dfrac{\partial}{\partial t}\boldsymbol{q}_{\mathrm{d}}+\dfrac{\partial}{\partial r}\boldsymbol{f}_{\mathrm{d}}(\boldsymbol{q}_{\mathrm{d}})+\dfrac{\partial}{\partial x}\boldsymbol{g}_{\mathrm{d}}(\boldsymbol{q}_{\mathrm{d}})=\boldsymbol{G}_{\mathrm{d}}, & (4.1\mathrm{b})\end{cases}$$

the second part, written in the form (3.2a), (3.2b), represents the drag effect between the two phases, and the third part, written in the form (3.3a), (3.3b), contains the heat transfer terms. As in the 1-D case, we denote solution operators for (4.1), (3.2) and (3.3) by $\mathcal{L}_0$, $\mathcal{L}_1$ and $\mathcal{L}_2$, respectively, and apply the second-order Strang operator splitting:

$$\boldsymbol{q}(r,z,t+\Delta t)\approx\mathcal{L}_0\Big(\frac{\Delta t}{2}\Big)\mathcal{L}_1\Big(\frac{\Delta t}{2}\Big)\mathcal{L}_2(\Delta t)\mathcal{L}_1\Big(\frac{\Delta t}{2}\Big)\mathcal{L}_0\Big(\frac{\Delta t}{2}\Big)\boldsymbol{q}(r,z,t). \tag{4.2}$$

In the following sections, we introduce the numerical schemes for the fluid dynamics (4.1a) and (4.1b), drag effect (3.2) and heat transfer (3.3) splitting steps.

4.1. $\mathcal{L}_0$: Fluid Dynamics Splitting Step

In this section, we introduce an FVP method for the uncoupled axisymmetric 3-D system (4.1). As in the 1-D case, the gas phase system (4.1a) is solved by a well-balanced CU scheme while the dust phase system (4.1b) is solved by the SP method.

4.1.1. *Well-Balanced Semi-Discrete Central-Upwind (CU) Scheme for the Gas Phase*

We start with a description of a semi-discrete well-balanced CU scheme for the system (4.1a). For simplicity, we partition the computational domain into uniform cells $C_{j,k}:=[r_{j-\frac{1}{2}},r_{j+\frac{1}{2}}]\times[z_{k-\frac{1}{2}},z_{k+\frac{1}{2}}]$ of size $|C_{j,k}|=\Delta r\Delta z$ centered at $(r_j,z_k)=((j+\frac{1}{2})\Delta r,k\Delta z)$, $j=0,\ldots,j_R$, $k=k_L,\ldots,k_R$. We assume

that at time level t, the cell averages of the numerical solution, $(\overline{\boldsymbol{q}_{\rm g}})_{j,k}(t) := \frac{1}{\Delta r\Delta z}\iint_{C_{j,k}} \boldsymbol{q}_{\rm g}(r,z,t)\,drdz$, are available.

In order to design a well-balanced CU scheme for the gas phase, we follow the approach from [9] and incorporate the gravitation term $-r\mathfrak{g}\rho_{\rm g}$ into the flux. To this end, we use the new variable w introduced in (2.16) and rewrite the gas part (4.1a) of the studied system as follows:

$$\frac{\partial}{\partial t}\boldsymbol{q}_{\rm g} + \frac{\partial}{\partial r}\boldsymbol{f}_{\rm g}(\boldsymbol{q}_{\rm g}) + \frac{\partial}{\partial z}\boldsymbol{g}_{\rm g}(\boldsymbol{q}_{\rm g}) = \boldsymbol{G}_{\rm g} + \boldsymbol{S}_r, \tag{4.3}$$

with

$$\boldsymbol{q}_{\rm g} = \begin{bmatrix} r\rho_{\rm g} \\ r\rho_{\rm g}u_{\rm g} \\ r\rho_{\rm g}v_{\rm g} \\ rE_{\rm g} \end{bmatrix}, \qquad \boldsymbol{f}_{\rm g}(\boldsymbol{q}_{\rm g}) = \begin{bmatrix} r\rho_{\rm g}u_{\rm g} \\ r(\rho_{\rm g}u_{\rm g}^2 + p_{\rm g}) \\ r\rho_{\rm g}u_{\rm g}v_{\rm g} \\ ru_{\rm g}(E_{\rm g} + p_{\rm g}) \end{bmatrix}, \qquad \boldsymbol{g}_{\rm g}(\boldsymbol{q}_{\rm g}) = \begin{bmatrix} r\rho_{\rm g}v_{\rm g} \\ r\rho_{\rm g}u_{\rm g}v_{\rm g} \\ r(\rho_{\rm g}v_{\rm g}^2 + w_{\rm g}) \\ rv_{\rm g}(E_{\rm g} + p_{\rm g}) \end{bmatrix}, \tag{4.4}$$

and

$$\boldsymbol{S}_r = \begin{bmatrix} 0 \\ p_{\rm g} \\ 0 \\ 0 \end{bmatrix}, \qquad \boldsymbol{G}_{\rm g} = \begin{bmatrix} 0 \\ 0 \\ 0 \\ -r\mathfrak{g}\rho_{\rm g}v_{\rm g} \end{bmatrix}. \tag{4.5}$$

A semi-discrete CU scheme from [33] applied to (4.3)–(4.5) results in the following system of ODEs:

$$\frac{d}{dt}(\overline{\boldsymbol{q}_{\rm g}})_{j,k} = -\frac{\boldsymbol{\mathcal{F}}_{j+\frac12,k} - \boldsymbol{\mathcal{F}}_{j-\frac12,k}}{\Delta r} - \frac{\boldsymbol{\mathcal{G}}_{j,k+\frac12} - \boldsymbol{\mathcal{G}}_{j,k-\frac12}}{\Delta z} + (\overline{\boldsymbol{G}_{\rm g}})_{j,k} + (\overline{\boldsymbol{S}_r})_{j,k}\,.$$

where

$$\begin{aligned}
\boldsymbol{\mathcal{F}}_{j+\frac12,k} &:= \frac{a^+_{j+\frac12,k}\boldsymbol{f}_{\rm g}\big((\boldsymbol{q}_{\rm g})^{\rm E}_{j,k}\big) - a^-_{j+\frac12,k}\boldsymbol{f}_{\rm g}\big((\boldsymbol{q}_{\rm g})^{\rm W}_{j+1,k}\big)}{a^+_{j+\frac12,k} - a^-_{j+\frac12,k}} \\
&\quad + \frac{a^+_{j+\frac12,k}a^-_{j+\frac12,k}}{a^+_{j+\frac12,k} - a^-_{j+\frac12,k}}(L_r)_{j+\frac12,k}\Big[(\boldsymbol{q}_{\rm g})^{\rm W}_{j+1,k} - (\boldsymbol{q}_{\rm g})^{\rm E}_{j,k}\Big], \\
\boldsymbol{\mathcal{G}}_{j,k+\frac12} &:= \frac{b^+_{j,k+\frac12}\boldsymbol{g}_{\rm g}\big((\boldsymbol{q}_{\rm g})^{\rm N}_{j,k}\big) - b^-_{j,k+\frac12}\boldsymbol{g}_{\rm g}\big((\boldsymbol{q}_{\rm g})^{\rm S}_{j,k+1}\big)}{b^+_{j,k+\frac12} - b^-_{j,k+\frac12}} \\
&\quad + \frac{b^+_{j,k+\frac12}b^-_{j,k+\frac12}}{b^+_{j,k+\frac12} - b^-_{j,k+\frac12}}(L_z)_{j,k+\frac12}\Big[(\boldsymbol{q}_{\rm g})^{\rm S}_{j+1,k} - (\boldsymbol{q}_{\rm g})^{\rm N}_{j,k}\Big]
\end{aligned} \tag{4.6}$$

are numerical fluxes. In what follows we provide explicit formulae for point values $(\boldsymbol{q}_{\rm g})^{\rm E(W,N,S)}_{j,k}$ computed at the middle of cell boundaries, matrices $(L_r)_{j+\frac12,k}$ and $(L_z)_{j,k+\frac12}$, and one-sided local propagation speeds, $a^\pm_{j+\frac12,k}$ and $b^\pm_{j+\frac12,k}$, across the lines $r = r_{j+\frac12}$ and $z = z_{k+\frac12}$, respectively.

In order to ensure the well-balanced property of the designed numerical method, we follow the idea from [9] and compute the one-sided point values of the conservative variables $(\boldsymbol{q}_{\rm g})^{\rm E(W,N,S)}_{j,k}$ in (4.6) in two steps: We first calculate the point values of the equilibrium variables $(\rho_{\rm g}, u_{\rm g}, v_{\rm g}, w_{\rm g})$ and then use them to obtain the point values of the conservative quantities $(r\rho_{\rm g}, r\rho u_{\rm g}, r\rho v_{\rm g}, rE_{\rm g})$. The former are

computed using the reconstruction operator $\mathcal{R}$ introduced in Appendix A.2 in (A.2):

$$
\begin{aligned}
&(\rho_{\mathrm{g}})^{\mathrm{E}}_{j,k} := \mathcal{R}\{(\rho_{\mathrm{g}})_{j,k}\}\big|_{r=r^-_{j+\frac{1}{2}},\, z=z_k}, && (\rho_{\mathrm{g}})^{\mathrm{W}}_{j,k} := \mathcal{R}\{(\rho_{\mathrm{g}})_{j,k}\}\big|_{r=r^+_{j-\frac{1}{2}},\, z=z_k},\\
&(\rho_{\mathrm{g}})^{\mathrm{N}}_{j,k} := \mathcal{R}\{(\rho_{\mathrm{g}})_{j,k}\}\big|_{r=r_j,\, z=z^-_{k+\frac{1}{2}}}, && (\rho_{\mathrm{g}})^{\mathrm{S}}_{j,k} := \mathcal{R}\{(\rho_{\mathrm{g}})_{j,k}\}\big|_{r=r_j,\, z=z^+_{k-\frac{1}{2}}},\\
&(u_{\mathrm{g}})^{\mathrm{E}}_{j,k} := \mathcal{R}\{(u_{\mathrm{g}})_{j,k}\}\big|_{r=r^-_{j+\frac{1}{2}},\, z=z_k}, && (u_{\mathrm{g}})^{\mathrm{W}}_{j,k} := \mathcal{R}\{(u_{\mathrm{g}})_{j,k}\}\big|_{r=r^+_{j-\frac{1}{2}},\, z=z_k},\\
&(u_{\mathrm{g}})^{\mathrm{N}}_{j,k} := \mathcal{R}\{(u_{\mathrm{g}})_{j,k}\}\big|_{r=r_j,\, z=z^-_{k+\frac{1}{2}}}, && (u_{\mathrm{g}})^{\mathrm{S}}_{j,k} := \mathcal{R}\{(u_{\mathrm{g}})_{j,k}\}\big|_{r=r_j, z=z^+_{k-\frac{1}{2}}},\\
&(v_{\mathrm{g}})^{\mathrm{E}}_{j,k} := \mathcal{R}\{(v_{\mathrm{g}})_{j,k}\}\big|_{r=r^-_{j+\frac{1}{2}}, z=z_k}, && (v_{\mathrm{g}})^{\mathrm{W}}_{j,k} := \mathcal{R}\{(v_{\mathrm{g}})_{j,k}\}\big|_{r=r^+_{j-\frac{1}{2}}, z=z_k},\\
&(v_{\mathrm{g}})^{\mathrm{N}}_{j,k} := \mathcal{R}\{(v_{\mathrm{g}})_{j,k}\}\big|_{r=r_j,\, z=z^-_{k+\frac{1}{2}}}, && (v_{\mathrm{g}})^{\mathrm{S}}_{j,k} := \mathcal{R}\{(v_{\mathrm{g}})_{j,k}\}\big|_{r=r_j,\, z=z^+_{k-\frac{1}{2}}},
\end{aligned}
\tag{4.7}
$$

where

$$
(\rho_{\mathrm{g}})_{j,k} = \frac{(\overline{r\rho_{\mathrm{g}}})_{j,k}}{r_j}, \quad (u_{\mathrm{g}})_{j,k} = \frac{(\overline{r\rho_{\mathrm{g}}u_{\mathrm{g}}})_{j,k}}{(\overline{r\rho_{\mathrm{g}}})_{j,k}}, \quad (v_{\mathrm{g}})_{j,k} = \frac{(\overline{r\rho_{\mathrm{g}}v_{\mathrm{g}}})_{j,k}}{(\overline{r\rho_{\mathrm{g}}})_{j,k}},
$$

are approximations of the cell center values of the gas density and velocities in the r- and z-directions, respectively.

Similarly, the one-sided point values of w are computed using the reconstruction operator $\mathcal{R}$ given by (A.2). It should be observed, however, that since the gravitational force is only acting vertically, the special reconstruction of w_{g} and the integration of ρ_{g} are only needed in the z-direction. As a result, the values of $(w_{\mathrm{g}})^{\mathrm{E\,(W)}}_{j,k}$ are not needed to be computed and $(w_{\mathrm{g}})^{\mathrm{N\,(S)}}_{j,k}$ are obtained from:

$$
(w_{\mathrm{g}})^{\mathrm{N}}_{j,k} = \mathcal{R}\{(w_{\mathrm{g}})_{j,k}\}\big|_{r=r_j,\, z=z^-_{k+\frac{1}{2}}}, \qquad (w_{\mathrm{g}})^{\mathrm{S}}_{j,k} = \mathcal{R}\{(w_{\mathrm{g}})_{j,k}\}\big|_{r=r_j,\, z=z^+_{k-\frac{1}{2}}},
$$

where the cell center values of w_{g} are computed according to its definition given in (2.17):

$$
(w_{\mathrm{g}})_{j,k} = (R_{\mathrm{g}})_{j,k} + (p_{\mathrm{g}})_{j,k}.
$$

Here, the cell center values of gas pressure $(p_{\mathrm{g}})_{j,k}$ are given by

$$
(p_{\mathrm{g}})_{j,k} = \frac{\gamma-1}{r_j}\left[(\overline{rE_{\mathrm{g}}})_{j,k} - \frac{(\overline{r\rho_{\mathrm{g}}})_{j,k}}{2}\Big((u_{\mathrm{g}})^2_{j,k} + (v_{\mathrm{g}})^2_{j,k}\Big)\right],
$$

and the values of $(R_{\mathrm{g}})_{j,k}$ are obtained by integrating the piecewise linear reconstruction of ρ_{g}:

$$
(R_{\mathrm{g}})_{j,k_L-\frac{1}{2}} = 0, \quad \begin{cases} (R_{\mathrm{g}})_{j,k+\frac{1}{2}} = (R_{\mathrm{g}})_{j,k-\frac{1}{2}} + \mathfrak{g}\,\Delta z\,(\overline{\rho_{\mathrm{g}}})_{j,k}, \\ (R_{\mathrm{g}})_{j,k} = (R_{\mathrm{g}})_{j,k-\frac{1}{2}} + \dfrac{\mathfrak{g}\,\Delta z}{2}\,(\overline{\rho_{\mathrm{g}}})_{j,k} - \dfrac{\mathfrak{g}\,(\Delta z)^2}{8}\dfrac{\partial}{\partial z}\mathcal{R}\{(\rho_{\mathrm{g}})_{j,k}\}\big|_{r=r_j, z=z_k}. \end{cases}
$$

Once all of the equilibrium variables are reconstructed, we proceed to the computation of the point values of the other variables needed in the flux evaluations (4.6). Using the values of $(R_{\mathrm{g}})_{j,k+\frac{1}{2}}$ and $(w_{\mathrm{g}})^{\mathrm{N\,(S)}}_{j,k}$, we can recover the gas pressure values at the centers of top and bottom cell interfaces by:

$$
(p_{\mathrm{g}})^{\mathrm{N}}_{j,k} = (w_{\mathrm{g}})^{\mathrm{N}}_{j,k} - (R_{\mathrm{g}})_{j,k+\frac{1}{2}}, \qquad (p_{\mathrm{g}})^{\mathrm{S}}_{j,k} = (w_{\mathrm{g}})^{\mathrm{S}}_{j,k} - (R_{\mathrm{g}})_{j,k-\frac{1}{2}},
$$

while at the centers of the other two cell interfaces the values of $(p_{\mathrm{g}})^{\mathrm{E}}_{j,k}$ and $(p_{\mathrm{g}})^{\mathrm{W}}_{j,k}$ are obtained using the reconstruction operator $\mathcal{R}$ given by (A.2):

$$
(p_{\mathrm{g}})^{\mathrm{E}}_{j,k} = \mathcal{R}\{(p_{\mathrm{g}})_{j,k}\}\big|_{r=r^-_{j+\frac{1}{2}}, z=z_k}, \quad (p_{\mathrm{g}})^{\mathrm{W}}_{j,k} = \mathcal{R}\{(p_{\mathrm{g}})_{j,k}\}\big|_{r=r^+_{j-\frac{1}{2}}, z=z_k}. \tag{4.8}
$$

Using (4.7), (4.8) and the equation of state (2.6), we thus obtain all of the necessary point values of $(\boldsymbol{q}_{\rm g})$:

$$(\boldsymbol{q}_{\rm g})^{\rm E}_{j,k} := r_{j+\frac{1}{2}}\cdot\Big[(\rho_{\rm g})^{\rm E}_{j,k},(\rho_{\rm g})^{\rm E}_{j,k}(u_{\rm g})^{\rm E}_{j,k},(\rho_{\rm g})^{\rm E}_{j,k}(v_{\rm g})^{\rm E}_{j,k},\frac{(p_{\rm g})^{\rm E}_{j,k}}{\gamma-1}+\frac{(\rho_{\rm g})^{\rm E}_{j,k}}{2}\big[((u_{\rm g})^{\rm E}_{j,k})^2+((v_{\rm g})^{\rm E}_{j,k})^2\big]\Big],$$

$$(\boldsymbol{q}_{\rm g})^{\rm W}_{j,k} := r_{j-\frac{1}{2}}\cdot\Big[(\rho_{\rm g})^{\rm W}_{j,k},(\rho_{\rm g})^{\rm W}_{j,k}(u_{\rm g})^{\rm W}_{j,k},(\rho_{\rm g})^{\rm W}_{j,k}(v_{\rm g})^{\rm W}_{j,k},\frac{(p_{\rm g})^{\rm W}_{j,k}}{\gamma-1}+\frac{(\rho_{\rm g})^{\rm W}_{j,k}}{2}\big[((u_{\rm g})^{\rm W}_{j,k})^2+((v_{\rm g})^{\rm W}_{j,k})^2\big]\Big],$$

$$(\boldsymbol{q}_{\rm g})^{\rm N}_{j,k} := r_{j}\cdot\Big[(\rho_{\rm g})^{\rm N}_{j,k},(\rho_{\rm g})^{\rm N}_{j,k}(u_{\rm g})^{\rm N}_{j,k},(\rho_{\rm g})^{\rm N}_{j,k}(v_{\rm g})^{\rm N}_{j,k},\frac{(p_{\rm g})^{\rm N}_{j,k}}{\gamma-1}+\frac{(\rho_{\rm g})^{\rm N}_{j,k}}{2}\big[((u_{\rm g})^{\rm N}_{j,k})^2+((v_{\rm g})^{\rm N}_{j,k})^2\big]\Big],$$

$$(\boldsymbol{q}_{\rm g})^{\rm S}_{j,k} := r_{j}\cdot\Big[(\rho_{\rm g})^{\rm S}_{j,k},(\rho_{\rm g})^{\rm S}_{j,k}(u_{\rm g})^{\rm S}_{j,k},(\rho_{\rm g})^{\rm S}_{j,k}(v_{\rm g})^{\rm S}_{j,k},\frac{(p_{\rm g})^{\rm S}_{j,k}}{\gamma-1}+\frac{(\rho_{\rm g})^{\rm S}_{j,k}}{2}\big[((u_{\rm g})^{\rm S}_{j,k})^2+((v_{\rm g})^{\rm S}_{j,k})^2\big]\Big].$$

Another important point in ensuring the well-balanced property of the CU scheme is related to the amount of the numerical viscosity in the numerical fluxes (4.6). The viscosity is controlled by two diagonal matrices $(L_r)_{j+\frac{1}{2},k}$ and $(L_z)_{j,k+\frac{1}{2}}$ (see [9]), which are given by

$$(L_r)_{j+\frac{1}{2},k}=\begin{bmatrix} H(\Delta(w_{\rm g})_{j+\frac{1}{2},k}) & 0 & 0 & 0\\ 0 & 1 & 0 & 0\\ 0 & 0 & 1 & 0\\ 0 & 0 & 0 & 1\end{bmatrix},\qquad (L_z)_{j,k+\frac{1}{2}}=\begin{bmatrix} H(\Delta(w_{\rm g})_{j,k+\frac{1}{2}}) & 0 & 0 & 0\\ 0 & 1 & 0 & 0\\ 0 & 0 & 1 & 0\\ 0 & 0 & 0 & 1\end{bmatrix},$$

where

$$\begin{aligned}\Delta(w_{\rm g})_{j+\frac{1}{2},k}&=\frac{|(w_{\rm g})_{j+1,k}-(w_{\rm g}))_{j,k}|}{\Delta r}\cdot\frac{r_{j_R+\frac{1}{2}}}{\max_{j,k}\{(w_{\rm g})_{j,k}\}},\\ \Delta(w_{\rm g})_{j,k+\frac{1}{2}}&=\frac{|(w_{\rm g}))_{j,k+1}-(w_{\rm g}))_{j,k}|}{\Delta z}\cdot\frac{z_{k_R+\frac{1}{2}}-z_{k_L-\frac{1}{2}}}{\max_{j,k}\{(w_{\rm g})_{j,k}\}}.\end{aligned}\tag{4.9}$$

Here, the smooth function H is designed to be very small when the computed solution is locally at (near) the hydrostatic steady state, and to be close to 1 elsewhere. The occurrence of the steady states is detected by a zero (or almost zero) value of $\Delta(w_{\rm g})_{j+\frac{1}{2},k}$ (or $\Delta(w_{\rm g})_{j,k+\frac{1}{2}}$). Thus, $H(\Delta(w_{\rm g}))$ should give a zero value when $\Delta(w_{\rm g})=0$ and give values close to 1 otherwise. In all of our numerical experiments, we have used a H function proposed in [9]:

$$H(\Delta(w_{\rm g}))=\frac{(C\Delta(w_{\rm g}))^m}{1+(C\Delta(w_{\rm g}))^m}$$

with the parameters $C=200$ and $m=6$. We also would like to point out that in (4.9), the approximate spatial derivatives of $w_{\rm g}$ are multiplied by factors $\frac{r_{j_R+\frac{1}{2}}}{\max_{j,k}\{(w_{\rm g})_{j,k}\}}$ and $\frac{z_{k_R+\frac{1}{2}}-z_{k_L-\frac{1}{2}}}{\max_{j,k}\{(w_{\rm g})_{j,k}\}}$, so to make the variables $\Delta(w_{\rm g})_{j+\frac{1}{2},k}$ and $\Delta(w_{\rm g})_{j,k+\frac{1}{2}}$ dimensionless.

Finally, the one-sided local speeds of propagation, $a^{\pm}_{j+\frac{1}{2},k}$ and $b^{\pm}_{j,k+\frac{1}{2}}$ are estimated using the smallest and largest eigenvalues of the Jacobians $\frac{\partial\boldsymbol{F}}{\partial\boldsymbol{q}_{\rm g}}$ and $\frac{\partial\boldsymbol{G}}{\partial\boldsymbol{q}_{\rm g}}$; see [22]:

$$\begin{aligned}a^{+}_{j+\frac{1}{2},k}&=\max\Big((u_{\rm g})^{\rm E}_{j,k}+(c_{\rm g})^{\rm E}_{j,k},\,(u_{\rm g})^{\rm W}_{j+1,k}+(c_{\rm g})^{\rm W}_{j+1,k},\,0\Big),\\ a^{-}_{j+\frac{1}{2},k}&=\min\Big((u_{\rm g})^{\rm E}_{j,k}-(c_{\rm g})^{\rm E}_{j,k},\,(u_{\rm g})^{\rm W}_{j+1,k}-(c_{\rm g})^{\rm W}_{j+1,k},\,0\Big),\\ b^{+}_{j,k+\frac{1}{2}}&=\max\Big((v_{\rm g})^{\rm N}_{j,k}+(c_{\rm g})^{\rm N}_{j,k},\,(v_{\rm g})^{\rm S}_{j,k+1}+(c_{\rm g})^{\rm S}_{j,k+1},\,0\Big),\\ b^{-}_{j,k+\frac{1}{2}}&=\min\Big((v_{\rm g})^{\rm N}_{j,k}-(c_{\rm g})^{\rm N}_{j,k},\,(v_{\rm g})^{\rm S}_{j,k+1}-(c_{\rm g})^{\rm S}_{j,k+1},\,0\Big),\end{aligned}\tag{4.10}$$

where the speeds of sound $(c_{\rm g})^{\rm E}_{j,k}, (c_{\rm g})^{\rm W}_{j+1,k}, (c_{\rm g})^{\rm N}_{j,k}$ and $(c_{\rm g})^{\rm S}_{j,k+1}$ are computed by

$$(c_{\rm g})^{\rm E}_{j,k} = \sqrt{\frac{\gamma (p_{\rm g})^{\rm E}_{j,k}}{(\rho_{\rm g})^{\rm E}_{j,k}}}, \quad (c_{\rm g})^{\rm W}_{j,k} = \sqrt{\frac{\gamma (p_{\rm g})^{\rm W}_{j,k}}{(\rho_{\rm g})^{\rm W}_{j,k}}}, \quad (c_{\rm g})^{\rm N}_{j,k} = \sqrt{\frac{\gamma (p_{\rm g})^{\rm N}_{j,k}}{(\rho_{\rm g})^{\rm N}_{j,k}}}, \quad (c_{\rm g})^{\rm S}_{j,k} = \sqrt{\frac{\gamma (p_{\rm g})^{\rm S}_{j,k}}{(\rho_{\rm g})^{\rm S}_{j,k}}}.$$

4.1.2. *Sticky Particle (SP) Method for the Dust Phase*

In this section, we describe the multidimensional SP method from [14], which is used to solve the dust phase system (4.1b). To this end, we seek a solution of (4.1b) in the form of linear combination of M δ-functions:

$$\boldsymbol{q}^M_{\rm d}(r,z,t) = \sum_{i=1}^{M} \boldsymbol{\alpha}_i(t)\delta(r - r^{\mathcal{P}}_i(t), z - z^{\mathcal{P}}_i(t)), \quad \boldsymbol{\alpha}_i = (\, r_i m_i, r_i m_i (u_{\rm d})_i, r_i m_i (v_{\rm d})_i, r_i (E_{\rm d})_i \,)^T, \quad (4.11)$$

where $(r^{\mathcal{P}}_i, z^{\mathcal{P}}_i)$ and $\boldsymbol{\alpha}_i$ denote the location and weights of the $i^{\rm th}$ particle that carries the mass $r_i m_i$, r-momentum $r_i m_i (u_{\rm d})_i$, z-momentum $r_i m_i (v_{\rm d})_i$ and energy $r_i (E_{\rm d})_i$.

The initial weights and locations of the particles are determined based on the initial conditions $\boldsymbol{q}_{\rm d}(r,z,0) = (r\rho_{\rm d}(r,z,0), r\rho_{\rm d} u(r,z,0), r\rho_{\rm d} v(r,z,0), rE_{\rm d}(r,z,0))^T$. First, the computational domain Ω is partitioned into M non-overlapping subdomains Ω^0_i, $i = 1,\ldots,M$, then the $i^{\rm th}$ particle with the weight $\boldsymbol{\alpha}_i(0) = \iint_{\Omega^0_i} \boldsymbol{q}_{\rm d}(r,z,0)\, drdz$ is placed at the geometric center of Ω^0_i denoted by $(r^{\mathcal{P}}_i(0), z^{\mathcal{P}}_i(0))$. For instance, one may choose $\{\Omega^0_i\}$ to be a uniform partition of Ω and $(r^{\mathcal{P}}_i(0), z^{\mathcal{P}}_i(0))$ to be the center of the cell Ω^0_i. Then, the particle weights are approximated by a midpoint quadrature:

$$\boldsymbol{\alpha}_i(0) = \iint\limits_{\Omega^0_i} \boldsymbol{q}_{\rm d}(r,z,0)\, drdz \approx |\Omega^0_i| \boldsymbol{q}_{\rm d}(r^{\mathcal{P}}_i(0), z^{\mathcal{P}}_i(0), 0).$$

Based on the weak formulation of (4.1b), the locations and weights of the particles are evolved according to the following ODEs; see [14]:

$$\frac{dr^{\mathcal{P}}_i(t)}{dt} = \widetilde{u_{\rm d}}(r^{\mathcal{P}}_i(t), z^{\mathcal{P}}_i(t), t), \quad \frac{dz^{\mathcal{P}}_i(t)}{dt} = \widetilde{v_{\rm d}}(r^{\mathcal{P}}_i(t), z^{\mathcal{P}}_i(t), t),$$
$$\frac{d\boldsymbol{\alpha}_i(t)}{dt} = \Big(0, 0, -\mathfrak{g}\alpha^{(1)}_i(t), -\mathfrak{g}\alpha^{(3)}_i(t)\Big)^T,$$

where $\widetilde{u_{\rm d}}(r,z,t)$ and $\widetilde{v_{\rm d}}(r,z,t)$ are two piecewise linear reconstructions of the dust velocities obtained in the following ways. First, we compute the average velocities of the particles, $(u_{\rm d})^{\rm CM}_{j,k}$ and $(v_{\rm d})^{\rm CM}_{j,k}$, which are computed by

$$(u_{\rm d})^{\rm CM}_{j,k} = \frac{\sum\limits_{i:(r^{\mathcal{P}}_i, z^{\mathcal{P}}_i)(t)\in C_{j,k}} \alpha^{(2)}_i(t)}{\sum\limits_{i:(r^{\mathcal{P}}_i, z^{\mathcal{P}}_i)(t)\in C_{j,k}} \alpha^{(1)}_i(t)}, \qquad (v_{\rm d})^{\rm CM}_{j,k} = \frac{\sum\limits_{i:(r^{\mathcal{P}}_i, z^{\mathcal{P}}_i)(t)\in C_{j,k}} \alpha^{(3)}_i(t)}{\sum\limits_{i:(r^{\mathcal{P}}_i, z^{\mathcal{P}}_i)(t)\in C_{j,k}} \alpha^{(1)}_i(t)},$$

and can be viewed as approximate dust velocity values at the corresponding centers of mass:

$$(u_{\rm d})^{\rm CM}_{j,k} \approx \widetilde{u_{\rm d}}(r^{\rm CM}_{j,k}, z^{\rm CM}_{j,k}, t), \qquad (v_{\rm d})^{\rm CM}_{j,k} \approx \widetilde{v_{\rm d}}(r^{\rm CM}_{j,k}, z^{\rm CM}_{j,k}, t),$$

where

$$r^{\rm CM}_{j,k} = \frac{\sum\limits_{i:(r^{\mathcal{P}}_i, z^{\mathcal{P}}_i)(t)\in C_{j,k}} r^{\mathcal{P}}_i(t)\ \alpha^{(1)}_i(t)}{\sum\limits_{i:(r^{\mathcal{P}}_i, z^{\mathcal{P}}_i)(t)\in C_{j,k}} \alpha^{(1)}_i(t)}, \qquad z^{\rm CM}_{j,k} = \frac{\sum\limits_{i:(r^{\mathcal{P}}_i, z^{\mathcal{P}}_i)(t)\in C_{j,k}} z^{\mathcal{P}}_i(t)\ \alpha^{(1)}_i(t)}{\sum\limits_{i:(r^{\mathcal{P}}_i, z^{\mathcal{P}}_i)(t)\in C_{j,k}} \alpha^{(1)}_i(t)}. \quad (4.12)$$

Then, we reconstruct the piecewise linear approximation of $u_{\rm d}$ and $v_{\rm d}$ as follows:

$$\widetilde{u_{\rm d}}(r,z,t)=\mathcal{R}^{\mathcal{P}}\{((u_{\rm d})^{\rm CM}_{j,k},r^{\rm CM}_{j,k},z^{\rm CM}_{j,k})\},\qquad \widetilde{v_{\rm d}}(r,z,t)=\mathcal{R}^{\mathcal{P}}\{((v_{\rm d})^{\rm CM}_{j,k},r^{\rm CM}_{j,k},z^{\rm CM}_{j,k})\},$$

where the reconstruction operator $\mathcal{R}^{\mathcal{P}}$ is introduced in Appendix B.2 in (B.1).

For each particle, in addition to evolving its location and weights, we also need to keep track of the volume $|\Omega_i|$ occupied by the particle (it will be used in the computation of the exchange terms, see §4.4). As in [11], we evolve $|\Omega_i(t)|$ by solving the following ODEs:

$$\frac{d}{dt}|\Omega_i(t)|=\Big(\frac{\partial\widetilde{u_{\rm d}}}{\partial r}(r_i^{\mathcal{P}}(t),z_i^{\mathcal{P}}(t),t)+\frac{\partial\widetilde{v_{\rm d}}}{\partial z}(r_i^{\mathcal{P}}(t),z_i^{\mathcal{P}}(t),t)\Big)\,|\Omega_i(t)|$$

subject to the initial conditions $|\Omega_i(0)|=|\Omega_i^0|$.

4.1.3. *Particle Merger*

In order to prevent particle clustering in a relatively small region, we use particle merger procedure similar to the 1-D one described in §3.1.3. Following [14] we choose a predetermined critical distance d_{cr} and force any two particles, say, the $i^{\rm th}$ and $j^{\rm th}$ ones, with the distance between them smaller than d_{cr} to be merged into a new particle with the following weights and locations:

$$\boldsymbol{\alpha}^{\rm new}=\boldsymbol{\alpha}_i+\boldsymbol{\alpha}_j,\qquad r^{\rm new}=\frac{m_ir_i^{\mathcal{P}}+m_jr_j^{\mathcal{P}}}{m_i+m_j},\qquad z^{\rm new}=\frac{m_iz_i^{\mathcal{P}}+m_jz_j^{\mathcal{P}}}{m_i+m_j}.$$

This procedure of particle merger is repeated until the distance between any pair of remaining particles is greater than d_{cr}.

4.1.4. *Particle Redistribution*

In order to prevent the particle distribution from becoming too sparse, we develop the following procedure (similar to the 1-D one presented in §3.1.4) to detect and locally redistribute isolated particles. First, the total number of particles located in the cell $C_{j,k}$ is counted and denoted by $n_{j,k}$. If one of the particle-occupied cells ($n_{j,k}>0$) has eight "empty" neighboring cells, then we regard the particles in this cell as isolated. We then replace all of the isolated particles in the computational domain with a new group of particles located at the centers of the FV cells $\{r_{\ell_1},z_{\ell_2}\}$ and carrying the weights $\{\boldsymbol{\alpha}_\ell^{\rm new}\}$ given by

$$\boldsymbol{\alpha}_\ell^{\rm new}=\sum_{i\in I}\Phi\Big(\frac{r_i^{\mathcal{P}}-r_\ell}{\Delta r}\Big)\Phi\Big(\frac{z_i^{\mathcal{P}}-z_\ell}{\Delta z}\Big)\boldsymbol{\alpha}_i,$$

where

$$I=\{\,i\mid(r_i^{\mathcal{P}},z_i^{\mathcal{P}})\in C_{j,k}:n_{j,k}>0,\ \sum_{j'=j-1}^{j+1}\sum_{k'=k-1}^{k+1}n_{j',k'}=n_{j,k}\}$$

and ϕ is the compactly supported function given by (3.15). As in the 1-D case, one can show this redistribution procedure is conservative, that is, equation (3.16) is satisfied.

4.2. $\mathcal{L}_1$: Interaction Time Step for Drag Effect

In this section, we describe the numerical scheme for solving the system (3.2) over the time interval $[t_0,t_0+\Delta t]$. We follow the 1-D approach described in §3.2 (see also [45]). Omitting the dependence

on r and z, we rewrite (3.2) in the following component wise form:

$$\begin{aligned}
&\frac{d}{dt}\rho_{\mathrm{g}}(t) = 0,\\
&\frac{d}{dt}\rho_{\mathrm{g}}\boldsymbol{\mathcal{V}}_{\mathrm{g}}(t) = -A\,|\boldsymbol{\mathcal{V}}_{\mathrm{g}}(t) - \boldsymbol{\mathcal{V}}_{\mathrm{d}}(t)|\,(\boldsymbol{\mathcal{V}}_{\mathrm{g}}(t) - \boldsymbol{\mathcal{V}}_{\mathrm{d}}(t)),\\
&\frac{d}{dt}E_{\mathrm{g}}(t) = -A\,|\boldsymbol{\mathcal{V}}_{\mathrm{g}}(t) - \boldsymbol{\mathcal{V}}_{\mathrm{d}}(t)|\,(\boldsymbol{\mathcal{V}}_{\mathrm{g}}(t) - \boldsymbol{\mathcal{V}}_{\mathrm{d}}(t))\cdot\boldsymbol{\mathcal{V}}_{\mathrm{d}}(t),\\
&\frac{d}{dt}\rho_{\mathrm{d}}(t) = 0,\\
&\frac{d}{dt}\rho_{\mathrm{d}}\boldsymbol{\mathcal{V}}_{\mathrm{d}}(t) = A\,|\boldsymbol{\mathcal{V}}_{\mathrm{g}}(t) - \boldsymbol{\mathcal{V}}_{\mathrm{d}}(t)|\,(\boldsymbol{\mathcal{V}}_{\mathrm{g}}(t) - \boldsymbol{\mathcal{V}}_{\mathrm{d}}(t)),\\
&\frac{d}{dt}E_{\mathrm{d}}(t) = A\,|\boldsymbol{\mathcal{V}}_{\mathrm{g}}(t) - \boldsymbol{\mathcal{V}}_{\mathrm{d}}(t)|\,(\boldsymbol{\mathcal{V}}_{\mathrm{g}}(t) - \boldsymbol{\mathcal{V}}_{\mathrm{d}}(t))\cdot\boldsymbol{\mathcal{V}}_{\mathrm{d}}(t).
\end{aligned} \tag{4.13}$$

As in the 1-D case, the ODE system (4.13) can be analytically solved. The average momenta and energy for the gas phase are then evolved over the time interval $[t_0, t_0 + \Delta t]$ by

$$\begin{aligned}
(\overline{r\rho_{\mathrm{g}}u_{\mathrm{g}}})_{j,k}(t_0+\Delta t) &= (\overline{r\rho_{\mathrm{g}}u_{\mathrm{g}}})_{j,k}(t_0) + r_j\,(M_1^{\mathrm{ex}})^{(1)}(r_j, z_k)\\
(\overline{r\rho_{\mathrm{g}}v_{\mathrm{g}}})_{j,k}(t_0+\Delta t) &= (\overline{r\rho_{\mathrm{g}}v_{\mathrm{g}}})_{j,k}(t_0) + r_j\,(M_1^{\mathrm{ex}})^{(2)}(r_j, z_k)\\
(\overline{rE_{\mathrm{g}}})_{j,k}(t_0+\Delta t) &= (\overline{rE_{\mathrm{g}}})_{j,k}(t_0) + r_j\,E_1^{\mathrm{ex}}(r_j, z_k),
\end{aligned} \tag{4.14}$$

while the momentum and energy weights of the ith particle for the dust phase are computed by

$$\begin{aligned}
\alpha^{(2)}(t_0+\Delta t) &= \alpha^{(2)}(t_0) + r_j^{\mathcal{P}}\,|\Omega_i|(M_1^{\mathrm{ex}})^{(1)}(r_i^{\mathcal{P}}, z_i^{\mathcal{P}}),\\
\alpha^{(3)}(t_0+\Delta t) &= \alpha^{(3)}(t_0) + r_j^{\mathcal{P}}\,|\Omega_i|(M_1^{\mathrm{ex}})^{(2)}(r_i^{\mathcal{P}}, z_i^{\mathcal{P}}),\\
\alpha^{(4)}(t_0+\Delta t) &= \alpha^{(4)}(t_0) + r_j^{\mathcal{P}}\,|\Omega_i|E_1^{\mathrm{ex}}(r_i^{\mathcal{P}}, z_i^{\mathcal{P}}).
\end{aligned} \tag{4.15}$$

Here, the momentum exchange $\boldsymbol{M}_1^{\mathrm{ex}}$ and energy exchange E_1^{ex} are obtained by

$$\boldsymbol{M}_1^{\mathrm{ex}} = \frac{\Delta\boldsymbol{\mathcal{V}}(t_0)}{\xi}\left(\frac{1}{\tau} - 1\right)$$

and

$$E_1^{\mathrm{ex}} = |\Delta\boldsymbol{\mathcal{V}}(t_0)|^3\,\frac{A\Delta t\,(1+\tau)}{2\xi\rho_{\mathrm{d}}(t_0)\tau^2} - \frac{A\Delta t}{\tau}\,|\Delta\boldsymbol{\mathcal{V}}(t_0)|\,\widehat{\boldsymbol{\mathcal{V}}}(t_0)\cdot\Delta\boldsymbol{\mathcal{V}}(t_0),$$

where

$$\Delta\boldsymbol{\mathcal{V}}(t_0) = \boldsymbol{\mathcal{V}}_{\mathrm{g}}(t_0) - \boldsymbol{\mathcal{V}}_{\mathrm{d}}(t_0), \qquad \widehat{\boldsymbol{\mathcal{V}}}(t_0) = \frac{\rho_{\mathrm{g}}(t_0)\boldsymbol{\mathcal{V}}_{\mathrm{g}}(t_0) + \rho_{\mathrm{d}}(t_0)\boldsymbol{\mathcal{V}}_{\mathrm{d}}(t_0)}{\rho_{\mathrm{g}}(t_0) + \rho_{\mathrm{d}}(t_0)},$$

$$\xi = \frac{1}{\rho_{\mathrm{g}}(t_0)} + \frac{1}{\rho_{\mathrm{d}}(t_0)}, \qquad \tau = 1 + A\,\xi|\Delta\boldsymbol{\mathcal{V}}(t_0)|\Delta t$$

and the coefficient A is computed at time $t = t_0$ using (2.12)–(2.14).

Note that the numerical solutions of the two phases are realized in different forms. As such, the exchanges terms in (4.14) and (4.15) are in fact computed at different locations (r_j, z_k) and $(r_i^{\mathcal{P}}, z_i^{\mathcal{P}})$. Similar to the 1-D case, a multidimensional version of the intergrid projection is needed here and will be introduced in (4.4) below.

4.3. $\mathcal{L}_2$: Interaction Time Step for Heat Transfer

In this section, we review the numerical scheme proposed in [45] for solving the system (3.3) over the time interval $[t_0, t_0 + \Delta t]$. Similarly to the 1-D scheme, described in §3.3, we omit the dependence on r and $z$and rewrite (3.3) in the component wise form:

$$\begin{aligned}
&\frac{d}{dt}\rho_{\rm g}(t) = 0,\\
&\frac{d}{dt}\rho_{\rm g}\boldsymbol{\mathcal{V}}_{\rm g}(t) = \mathbf{0},\\
&\frac{d}{dt}E_{\rm g}(t) = -Q\,\left(T_{\rm g}(t) - T_{\rm d}(t)\right),\\
&\frac{d}{dt}\rho_{\rm d}(t) = 0,\\
&\frac{d}{dt}\rho_{\rm d}\boldsymbol{\mathcal{V}}_{\rm d}(t) = \mathbf{0},\\
&\frac{d}{dt}E_{\rm d}(t) = Q\,\left(T_{\rm g}(t) - T_{\rm d}(t)\right).
\end{aligned} \tag{4.16}$$

Similar to the 1-D case, the system (4.16) can also be analytically solved, leading to the following formulae used to evolve the gas and dust energies over the time interval $[t_0, t_0 + \Delta t]$. For the gas phase, the energy is updated by

$$(\overline{rE_{\rm g}})_{j,k}(t_0 + \Delta t) = (\overline{rE_{\rm g}})_{j,k}(t_0) + r_j\, E_2^{\rm ex}(r_j, z_k), \tag{4.17}$$

and for the dust phase, the energy weight of the $i^{\rm th}$ particle is evolved by

$$\alpha_i^{(4)}(t_0 + \Delta t) = \alpha_i^{(4)}(t_0) + r_i^{\mathcal{P}}\,|\Omega_i(t_0)|E_2^{\rm ex}(r_i^{\mathcal{P}}, z_i^{\mathcal{P}}). \tag{4.18}$$

Here, the energy exchange $E_2^{\rm ex}$ is computed by

$$E_2^{\rm ex} = \frac{T_{\rm g}(t_0) - T_{\rm d}(t_0)}{\eta}\left[e^{-Q\,\eta\,\Delta t} - 1\right],$$

where

$$\eta = \frac{(\gamma - 1)}{\rho_{\rm g}} + \frac{R}{\rho_{\rm d} c_{\rm vd}}$$

and the coefficient Q is computed at time $t = t_0$ using (2.12)–(2.14).

Note that in (4.17) and (4.18), the computations of $E_2^{\rm ex}$ require the densities and temperatures of both phases at both (r_j, z_k) and $(r_i^{\mathcal{P}}, z_i^{\mathcal{P}})$. In the next section, we will introduce how to obtain those values by projecting the FV data onto the particle locations and the particle data onto the cell centers.

4.4. Finite-Volume and Particle Data Projection

Here, we describe multidimensional techniques which are used to project the FV data onto the set of particle locations $\{(r_i^{\mathcal{P}}(t), z_i^{\mathcal{P}}(t))\}$ and the particle data onto the cell centers $\{(r_j, z_k)\}$. We assume that the gas- and dust-phase numerical solutions, namely, $\{(\overline{\boldsymbol{q}_{\rm g}})_{j,k}(t)\}$ and $\{\boldsymbol{\alpha}_i(t), r_i^{\mathcal{P}}(t), z_i^{\mathcal{P}}(t)\}$, are available at a certain time level t.

First, to evaluate the dust data at the cell centers, we use the piecewise linear reconstruction operator $\mathcal{R}^{\mathcal{P}}$ to obtain (see Appendix B.2):

$$\rho_{\rm d}(r_j,z_k,t) = \mathcal{R}^{\mathcal{P}}\left\{\left(\frac{1}{\Delta r\Delta z}\sum_{i:(r_i,z_i)^{\mathcal{P}}\in C_{j,k}}\alpha_i^{(1)}(t), r_{j,k}^{\rm CM}, z_{j,k}^{\rm CM}\right)\right\}\Bigg|_{r=r_j,z=z_k},$$

$$u_{\rm d}(r_j,z_k,t) = \mathcal{R}^{\mathcal{P}}\left\{\left(\frac{\sum_{i:(r_i,z_i)^{\mathcal{P}}\in C_{j,k}}\alpha_i^{(2)}(t)}{\sum_{i:(r_i,z_i)^{\mathcal{P}}\in C_{j,k}}\alpha_i^{(1)}(t)}, r_{j,k}^{\rm CM}, z_{j,k}^{\rm CM}\right)\right\}\Bigg|_{r=r_j,z=z_k},$$

$$v_{\rm d}(r_j,z_k,t) = \mathcal{R}^{\mathcal{P}}\left\{\left(\frac{\sum_{i:(r_i,z_i)^{\mathcal{P}}\in C_{j,k}}\alpha_i^{(3)}(t)}{\sum_{i:(r_i,z_i)^{\mathcal{P}}\in C_{j,k}}\alpha_i^{(1)}(t)}, r_{j,k}^{\rm CM}, z_{j,k}^{\rm CM}\right)\right\}\Bigg|_{r=r_j,z=z_k},$$

$$T_{\rm d}(r_j,z_k,t) = \mathcal{R}^{\mathcal{P}}\left\{(T_{j,k}^{\rm CM}, r_{j,k}^{\rm CM}, z_{j,k}^{\rm CM})\right\}\Big|_{r=r_j,z=z_k}.$$

where

$$T_{j,k}^{\rm CM} = \frac{R}{c_{\rm vd}}\left[\frac{\sum_{i:(r_i,z_i)^{\mathcal{P}}\in C_{j,k}}\alpha_i^{(4)}(t)}{\sum_{i:(r_i,z_i)^{\mathcal{P}}\in C_{j,k}}\alpha_i^{(1)}(t)} - \frac{1}{2}\left(\frac{\sum_{i:(r_i,z_i)^{\mathcal{P}}\in C_{j,k}}\alpha_i^{(2)}(t)}{\sum_{i:(r_i,z_i)^{\mathcal{P}}\in C_{j,k}}\alpha_i^{(1)}(t)}\right)^2 - \frac{1}{2}\left(\frac{\sum_{i:(r_i,z_i)^{\mathcal{P}}\in C_{j,k}}\alpha_i^{(3)}(t)}{\sum_{i:(r_i,z_i)^{\mathcal{P}}\in C_{j,k}}\alpha_i^{(1)}(t)}\right)^2\right]$$

and $(r_i^{\rm CM}, z_i^{\rm CM})$ are the centers of mass of the particles located in the cell $C_{j,k}$; see (4.12).

Using the reconstruction operator $\mathcal{R}$ (see Appendix A.2), we then project the gas data onto the set of particle locations:

$$\rho_{\rm g}(r_i^{\mathcal{P}}(t), z_i^{\mathcal{P}}(t), t) = \mathcal{R}\left\{(\overline{\rho_{\rm g}})_{j,k}(t)\right\}(r_i^{\mathcal{P}}, z_i^{\mathcal{P}}), \qquad T_{\rm g}(r_i^{\mathcal{P}}(t), z_i^{\mathcal{P}}(t), t) = \mathcal{R}\left\{(T_{\rm g})_{j,k}(t)\right\}(r_i^{\mathcal{P}}, z_i^{\mathcal{P}}),$$

$$u_{\rm g}(r_i^{\mathcal{P}}(t), z_i^{\mathcal{P}}(t), t) = \mathcal{R}\left\{(u_{\rm g})_{j,k}(t)\right\}(r_i^{\mathcal{P}}, z_i^{\mathcal{P}}), \qquad v_{\rm g}(r_i^{\mathcal{P}}(t), z_i^{\mathcal{P}}(t), t) = \mathcal{R}\left\{(u_{\rm g})_{j,k}(t)\right\}(r_i^{\mathcal{P}}, z_i^{\mathcal{P}}),$$

where

$$(u_{\rm g})_{j,k}(t) = \frac{(\overline{r\rho_{\rm g}u_{\rm g}})_{j,k}(t)}{(\overline{r\rho_{\rm g}})_{j,k}(t)}, \qquad (v_{\rm g})_{j,k}(t) = \frac{(\overline{r\rho_{\rm g}v_{\rm g}})_{j,k}(t)}{(\overline{r\rho_{\rm g}})_{j,k}(t)},$$

$$(T_{\rm g})_{j,k}(t) = (\gamma-1)\left[\frac{(\overline{rE_{\rm g}})_{j,k}(t)}{(\overline{r\rho_{\rm g}})_{j,k}(t)} - \frac{(u_{\rm g})_{j,k}^2(t) + (v_{\rm g})_{j,k}^2(t)}{2}\right].$$

5. **Numerical Examples**

In the section, we test the performance of the designed hybrid FVP method. Among the three solution operators, $\mathcal{L}_0$, $\mathcal{L}_1$ and $\mathcal{L}_2$, the time step restrictions should only be considered for the $\mathcal{L}_0$ step, in which the numerical solutions of the gas and dust phases are evolved using the CU scheme and SP method, respectively. As described in §3 and §4, both the CU scheme and SP method result in time-dependent ODE systems, which should be integrated in time using a stable and accurate ODE solver. In the numerical examples reported below, we have used the three-stage third-order strong stability preserving (SSP) Runge-Kutta method; see, e.g.,[23, 24, 52].

For the CU scheme, the time step $\Delta t_{\rm g}$ is to be restricted by the CFL condition. We have used the CFL number 0.5 in the 1-D case:

$$\Delta t_{\rm g} = \frac{0.5\Delta x}{a}, \quad a = \max_j\left\{a_{j+\frac{1}{2}}^+, -a_{j+\frac{1}{2}}^-\right\},$$

where $a^{\pm}_{j+\frac{1}{2}}$ are the local propagation speeds defined in (3.9), and 0.4 in the axisymmetric 3-D case:

$$\Delta t_{\rm g} = 0.4\min\left\{\frac{\Delta r}{a},\frac{\Delta z}{b}\right\},\quad a=\max_{j,k}\left\{a^{+}_{j+\frac{1}{2},k},-a^{-}_{j+\frac{1}{2},k}\right\},\quad b=\max_{j,k}\left\{b^{+}_{j,k+\frac{1}{2}},-b^{-}_{j,k+\frac{1}{2}}\right\},\tag{5.1}$$

where $a^{\pm}_{j+\frac{1}{2},k}$ and $b^{\pm}_{j,k+\frac{1}{2}}$ are the local propagation speeds defined in (4.10). For the SP method, the time step $\Delta t_{\rm d}$ is to be chosen to avoid the trajectories of particles to intersect within one time step and we therefore use the following formulae for $\Delta t_{\rm d}$:

$$\Delta t_{\rm d}=\frac{1}{2}\min_{i}\left\{\frac{\min\limits_{i'\neq i}|x^{\mathcal{P}}_{i}(t)-x^{\mathcal{P}}_{i'}(t)|}{|u_{\rm d}(x^{\mathcal{P}}_{i}(t),t)|}\right\}$$

in the 1-D case, and

$$\Delta t_{\rm d}=\frac{1}{2}\min_{i}\left\{\sqrt{\frac{\min\limits_{i'\neq i}\left\{(r^{\mathcal{P}}_{i}(t)-r^{\mathcal{P}}_{i'}(t))^2+(z^{\mathcal{P}}_{i}(t)-z^{\mathcal{P}}_{i'}(t))^2\right\}}{u^2_{\rm d}(x^{\mathcal{P}}_{i}(t),t)+v^2_{\rm d}(x^{\mathcal{P}}_{i}(t),t)}}\right\}$$

in the axisymmetric 3-D case. We then select the following splitting time step in (3.4) and (4.2):

$$\Delta t=2\min(\Delta t_{\rm d},\Delta t_{\rm g}).$$

It should be pointed out that one can prove that the computed gas densities are guaranteed to remain nonnegative (the proof is similar to the proof of nonnegativity of the water depth computed by the CU scheme for the Saint-Venant system of shallow water equations; see, e.g., [31]). In the axisymmetric 3-D case, the positivity of $\rho_{\rm g}$ is theoretically ensured if the CFL number, which is 0.4 in (5.1), is replaced by 0.25. In our numerical experiments, however, we have still used a larger CFL number and never obtained negative values of the computed gas density. The dust densities computed by the SP method are naturally nonnegative (the only step at which one needs to be careful is the particle redistribution, but the weights in (3.14) are nonnegative since the function Φ given by (3.15) is nonnegative). On the other hand, the positivity of the gas pressure computed by the CU scheme cannot be guaranteed, but in the studied numerical examples no negative pressure values have been observed.

In all of the reported numerical experiments, we have used the minmod parameter $\theta=1.3$ for both reconstruction operators $\mathcal{R}$ and $\mathcal{R}^{\mathcal{P}}$, see Appendices A and B, respectively.

In Examples 1–5, we compare the results obtained by the proposed hybrid FVP method with those computed by a FV method, which was designed by applying the CU scheme to both the gas and dust phase systems.

5.1. **One-Dimensional Examples**

We begin with the 1-D numerical examples, in which we have used the following parameter values:

$$\gamma=1.4,\ d_{\rm p}=10^{-5},\ Pr=0.75,\ \rho_{\rm ref}=1.225,\ u_{\rm ref}=287.6,\ T_{\rm ref}=288.15.$$

We note that the dust phase numerical solution is realized in terms of particle distributions (3.10) and therefore we need to recover the corresponding point values to present the results obtained by the proposed FVP method. To this end, we use the same technique as the one used to redistribute particles in §3.1.4. The latter is now applied to all of the particles rather than to the isolated ones as

in §3.1.4. This way, we obtain the cell averages of $\rho_{\rm d}$, $\rho_{\rm d}u_{\rm d}$ and $E_{\rm d}$:

$$(\overline{\rho_{\rm d}})_j = \frac{1}{\Delta x}\sum_{i=1}^{M}\Phi\Big(\frac{x_i^{\mathcal{P}}-x_\ell}{\Delta x}\Big)\alpha_i^{(1)}, \qquad (\overline{\rho_{\rm d}u_{\rm d}})_j = \frac{1}{\Delta x}\sum_{i=1}^{M}\Phi\Big(\frac{x_i^{\mathcal{P}}-x_\ell}{\Delta x}\Big)\alpha_i^{(2)},$$
$$(\overline{E_{\rm d}})_j = \frac{1}{\Delta x}\sum_{i=1}^{M}\Phi\Big(\frac{x_i^{\mathcal{P}}-x_\ell}{\Delta x}\Big)\alpha_i^{(3)},$$

and then the point values of the velocity $(u_{\rm d})_j$ and temperature $(T_{\rm d})_j$ are obtained by

$$(u_{\rm d})_j = \frac{(\overline{\rho_{\rm d}u_{\rm d}})_j}{(\overline{\rho_{\rm d}})_j} \quad \text{and} \quad (T_{\rm d})_j = (\gamma-1)\Big(\frac{(\overline{E_{\rm d}})_j}{(\overline{\rho_{\rm d}})_j} - (u_{\rm d})_j^2\Big).$$

Example 1—Dusty Gas Shock Tube Problem. In this example, we consider a dusty gas shock tube problem introduced in [50]. The numerical experiments are conducted over the domain $[0,100]$ and the initial conditions are

$$\big(\rho_{\rm g}(x,0),u_{\rm g}(x,0),T_{\rm g}(x,0),\rho_{\rm d}(x,0),u_{\rm d}(x,0),T_{\rm d}(x,0)\big) = \begin{cases}(10,0,1,10^{-4},0,1), & x\le 40,\\ (1,0,1,1,0,1), & x>40.\end{cases}$$

We use $N=1000$ uniform cells and $M=1000$ particles for the hybrid FVP method. The snapshots of the computed solutions at times $t=5,10,30$ are shown in Figures 5.1. The results obtained by the designed FVP method are in good agreement with the results reported in [45] and [50], except for a spiky structure developed by the dust density at the gas contact wave region. To see this, we take a closer look at this region and compare the dust densities at $t=30$ computed by the FVP and FV methods with different resolutions with $N=M=1000,2000,4000$ and 8000. The obtained results are shown in Figure 5.2. As one can see, the spiky structure is much sharper resolved by the FVP method: to achieve a comparable resolution with the FV method, one needs to use about 8 times finer mesh and 4 times larger CPU time.

Remark 5.1. We would like to emphasize that the data on the CPU times in Figure 5.2 are provided for illustration purposes only since the designed FVP and FV codes were not optimized for a fair CPU time comparison. In particular, an efficient implementation of the FVP method would require the development of fast summation and search techniques, which is left for the future work. The purpose of showing the CPU times in this paper was to demonstrate that (i) for a given resolution, the FVP method would be more computationally expensive; (ii) the FVP method still outperforms the FV one since a much finer grid would be required for the FV method to achieve the results comparable to low resolution FVP computations.

Example 2—Dusty Gas Shock Tube Problem with Dust-Free Regions. We now consider the same setting as in Example 1, but take the dust density on the left to be zero, namely, we set $\rho_{\rm d}(x,0)=0$ for $x\le 40$.

In this setting, the application of the FVP method is straightforward: no particles are needed to be placed into the dust-free region at $t=0$. On contrary, when the FV method is applied, the computation of the dust velocities has to be desingularized to avoid division by zero (or very small) dust densities. To this end, we implement the desingularization technique from [10, 31] and compute the quantity $1/\rho_{\rm d}$ as follows:

$$\frac{1}{\rho_{\rm d}} \approx \frac{2\rho_{\rm d}}{\rho_{\rm d}^2+\max(\rho_{\rm d}^2,\varepsilon^2)},$$

where the parameter ε stands for a small density value, regarded as extremely dilute dust density.

In Figure 5.3, we compare the dust components of the solutions at time $t=30$ computed by the FVP method and the FV method applied to the entire system (3.1). We use four different values of ε

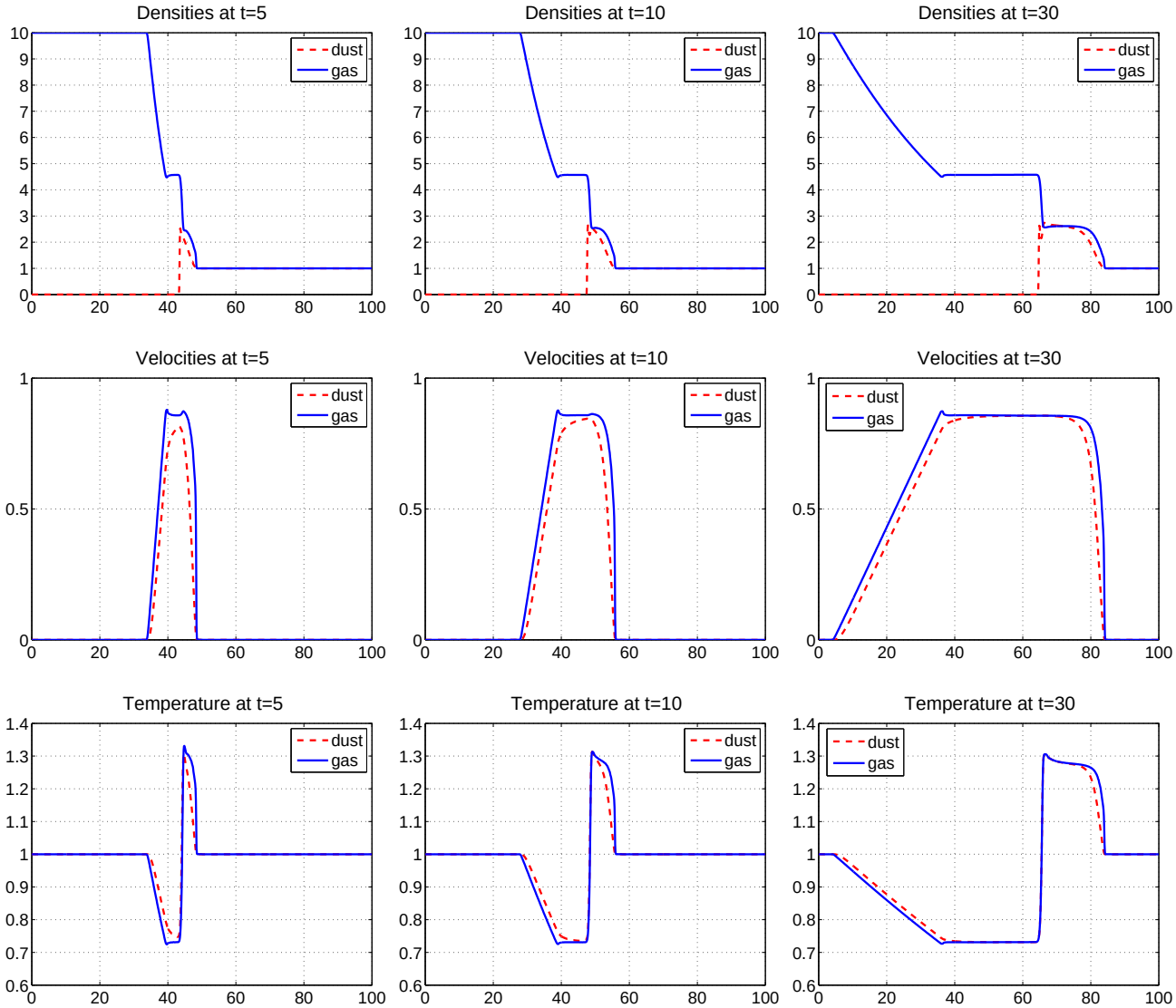

Figure 5.1. Example 1: The solutions (densities, velocities and temperatures of the both phases) at $t = 5, 10, 30$ computed by the FVP method.

and the same resolution by taking $N = 1000$ and $M = 600$ with the particles initially uniformly placed in the region $x \in [40, 100]$. As one can see, the discontinuity of dust density is dramatically effected by the numerical diffusion present in the FV method, while the dust density solution computed by FVP method provides a sharp resolution at the boundary of the dust-free region. Also, at the smeared discontinuity, the dust velocity and temperature obtained by the FV method appear to be very sensitive to the choice of the desingularization parameter ε.

5.2. **Axisymmetric Three-Dimensional Examples**

We now proceed with the axisymmetric 3-D numerical examples. As it is shown below, the numerical solutions realized in the form of particles clearly demonstrate the low dissipative nature of the FVP method. The latter enables the users to reveal the phenomenon of dust clustering, that is, certain

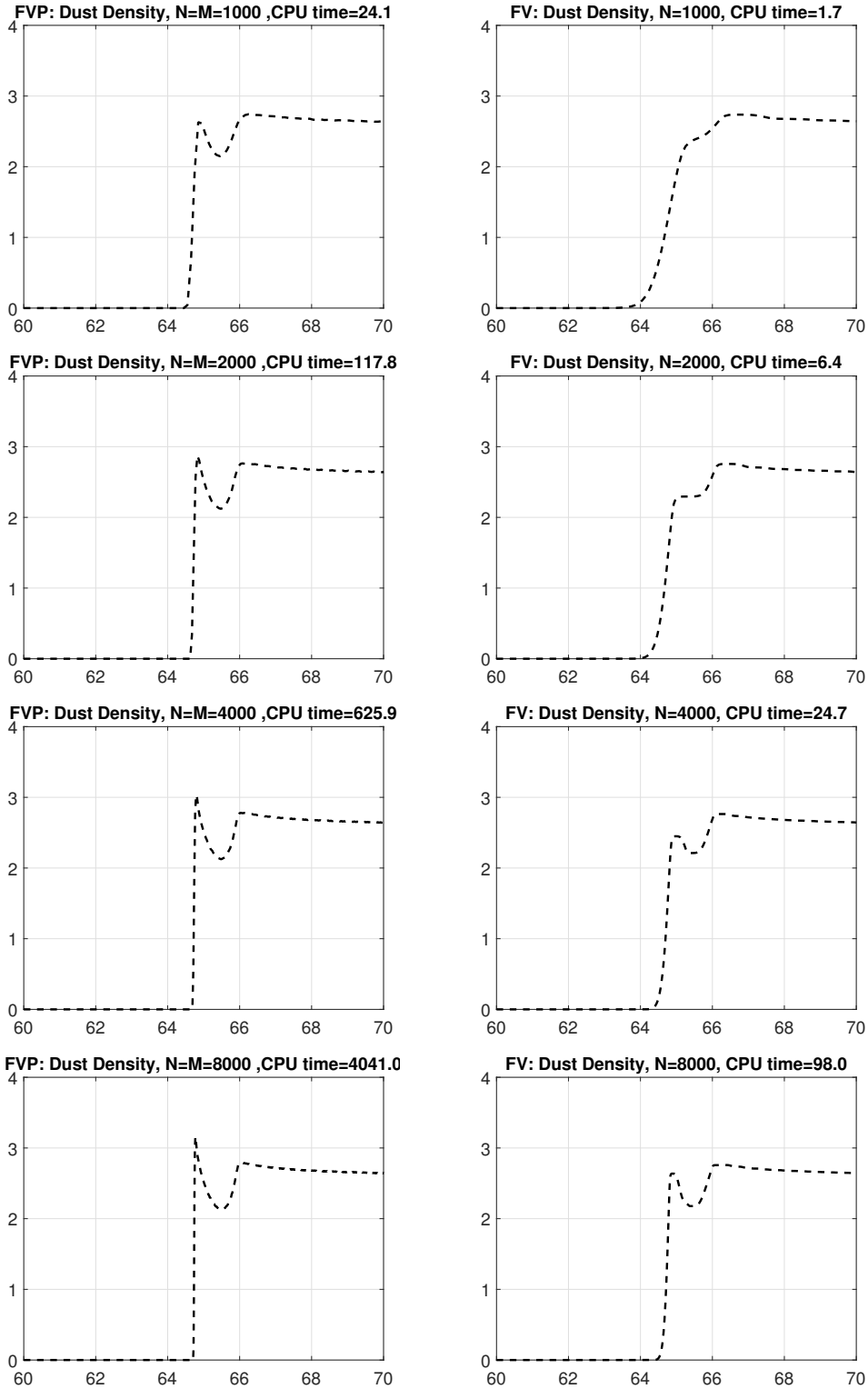

Figure 5.2. Example 1: Dust densities at $t = 30$ obtained by the FVP (left column) and FV (right column) methods using four different grids.

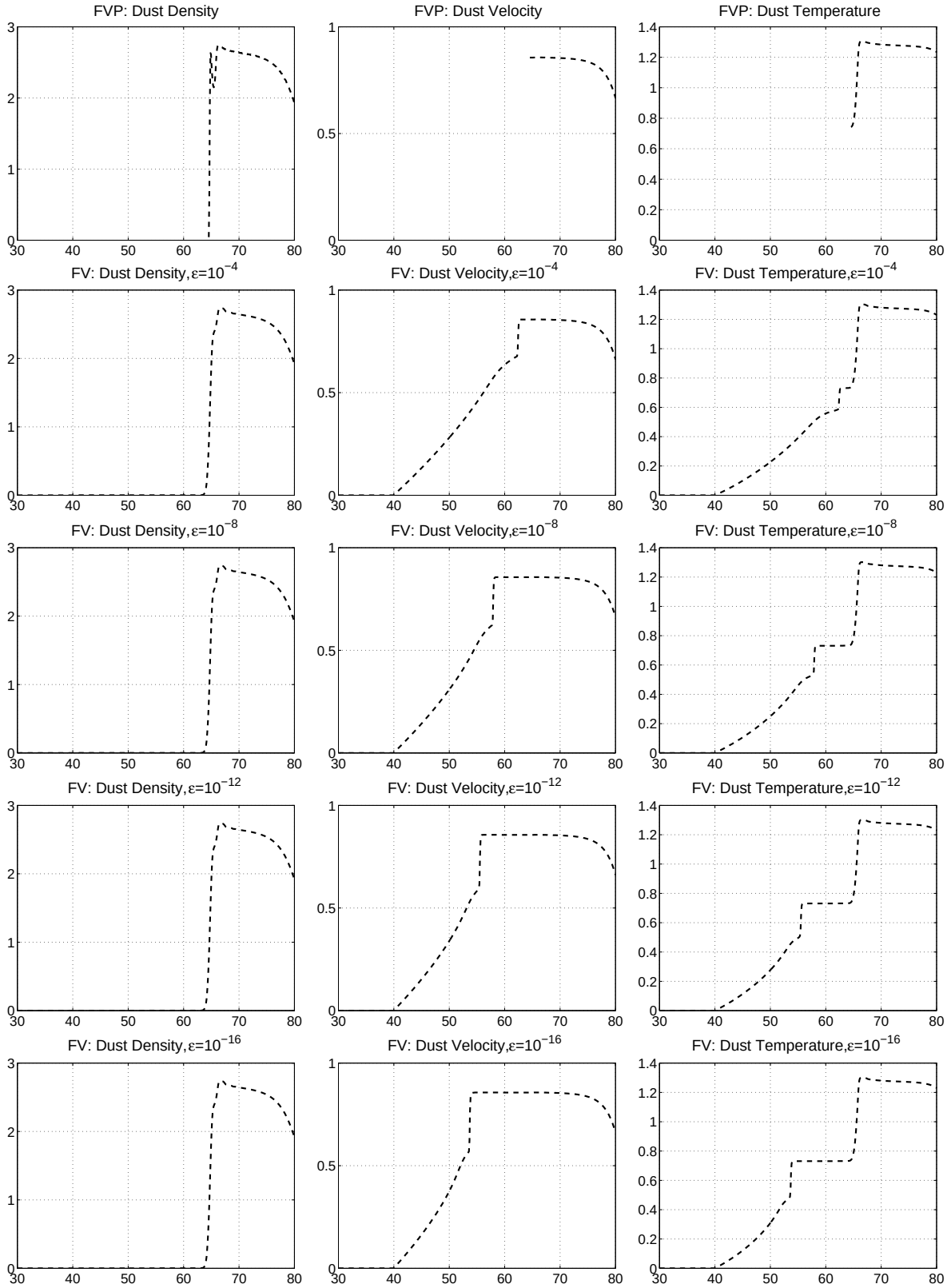

Figure 5.3. Example 2: The dust density, velocity and temperature obtained by the FVP method (first row) and the FV methods with four different values of ε.

amount of dust quantity concentrated in a very small space, resulting in an isolated region with relatively high density. It is well-known that such structures are developed by the solutions to the pressureless gas dynamic system; see, e.g., [14, 35] and references therein. We note that these singular structures are extremely hard to accurately capture by FV methods due to the inevitable numerical viscosity; see, e.g., [14].

The particles may also expand in space and the dust density will be then diluted. In order to capture the expansion and dilution process by the numerical approximation realized in terms of the particle distribution (4.11), we include the particle redistribution technique introduced in §4.1.4, by which the dust mass carried by isolated particles is relocated over nearby regions.

In order to recover the point values of the computed dust phase numerical solution from its particle distributions (4.11), we use the the same redistribution technique mentioned above in a collective way, that is, instead of focusing on isolated particles, we redistribute all of the particles and obtain a numerical solution defined on the center of grid cells. To this end, we first obtain the cell averages for the dust phase quantities:

$$(\overline{\boldsymbol{q}_{\rm d}})_{j,k} = \frac{1}{\Delta r \Delta z} \sum_{i=1}^{M} \Phi\Big(\frac{r_i^{\mathcal{P}} - r_j}{\Delta x}\Big)\Phi\Big(\frac{z_i^{\mathcal{P}} - z_k}{\Delta x}\Big)\boldsymbol{\alpha}_i, \tag{5.2}$$

where the function Φ is given in (3.15), and then compute the point values of the velocities $(u_{\rm d})_{j,k}$, $(v_{\rm d})_{j,k}$ and temperature $(T_{\rm g})_{j,k}$ as follows:

$$(u_{\rm d})_{j,k} = \frac{(\overline{r\rho_{\rm d} u_{\rm d}})_{j,k}}{(\overline{r\rho_{\rm d}})_{j,k}}, \quad (v_{\rm d})_{j,k} = \frac{(\overline{r\rho_{\rm d} v_{\rm d}})_{j,k}}{(\overline{r\rho_{\rm d}})_{j,k}}, \quad (T_{\rm d})_{j,k} = \frac{R}{c_{\rm vd}}\Big(\frac{(\overline{rE_{\rm d}})_{j,k}}{(\overline{r\rho_{\rm d}})_{j,k}} - \frac{1}{2}\Big((u_{\rm d})_{j,k}^2 + (v_{\rm d})_{j,k}^2\Big)\Big).$$

We have used the following parameters:

$$R = 287,\ \gamma = 1.4,\ c_{\rm vd} = 1.3 \times 10^3,\ \mu = 10^{-5},\ \kappa_{\rm g} = 0.05,\ d_{\rm p} = 10^{-5},$$

and reference values for density, velocity, temperature and pressure:

$$\rho_{\rm ref} = 1.225,\ u_{\rm ref} = 287.6,\ T_{\rm ref} = 288.15,\ p_{\rm ref} = 101325.$$

Following [45], we have also used the characteristic length $\ell = \frac{4\rho_{\rm p} d_{\rm p}}{3\rho_{\rm ref}}$ and characteristic time $\tau = \frac{\ell}{u_{\rm ref}}$ with the density of particle $\rho_{\rm p} = 2300$. Finally, the gravitation constant used here is given by $\mathfrak{g} = 9.8\tau/u_{\rm ref}$.

Example 3—Collapsing column. We first consider an example which simulates a cylindrical dusty gas column that falls down due to gravitation. Initially, the computational domain $(r, z) \in [0, 1000/\ell] \times [0, 700/\ell]$ is divided into two regions, respectively filled by pure gas and dusty gas:

$$(\rho_{\rm g}, u_{\rm g}, v_{\rm g}, T_{\rm g}, \rho_{\rm g}, u_{\rm g}, v_{\rm g}, T_{\rm g})\Big|_{(r,z,0)} = \begin{cases} (0.99, 0, 0, 1 - \mathfrak{g}z, 23, 0, 0, 1 - \mathfrak{g}z), & (r,z) \in \Big[0, \dfrac{200}{\ell}\Big] \times \Big[0, \dfrac{500}{\ell}\Big], \\ (1, 0, 0, 1 - \mathfrak{g}z, 0, 0, 0, 0), & \text{otherwise.} \end{cases}$$

We implement reflective boundary conditions on the boundaries of $r = 0$ and $z = 0$ and free boundary conditions on the two other boundaries, $r = 1000/\ell$ and $z = 700/\ell$.

In Figure 5.4, we compare the solutions (the dust density) computed at times $t = 5/\tau$, $10/\tau$ by both the FVP and FV methods implemented on a uniform grid with $N_r = 200$ and $N_z = 140$. For the FVP method particles are initially placed at the centers of the FV cells only in the region where dust density is positive and the critical distance $d_{cr} = \Delta r/2$ was used in the particle merger procedure. As one can see, the results obtained by the FVP method are less effected by the numerical diffusion and provide more details in small scales. In Figure 5.5, we show the results obtained by both the FVP and FV methods with a higher resolution ($N_r = 400, N_z = 280$). As one can see, the FVP results are much sharper than those obtained by the FV method. Moreover, the 200×140 FVP results computed

using the CPU time of $352s$ are comparable with the 400×280 FV results obtained using substantially larger CPU time of $2073s$.

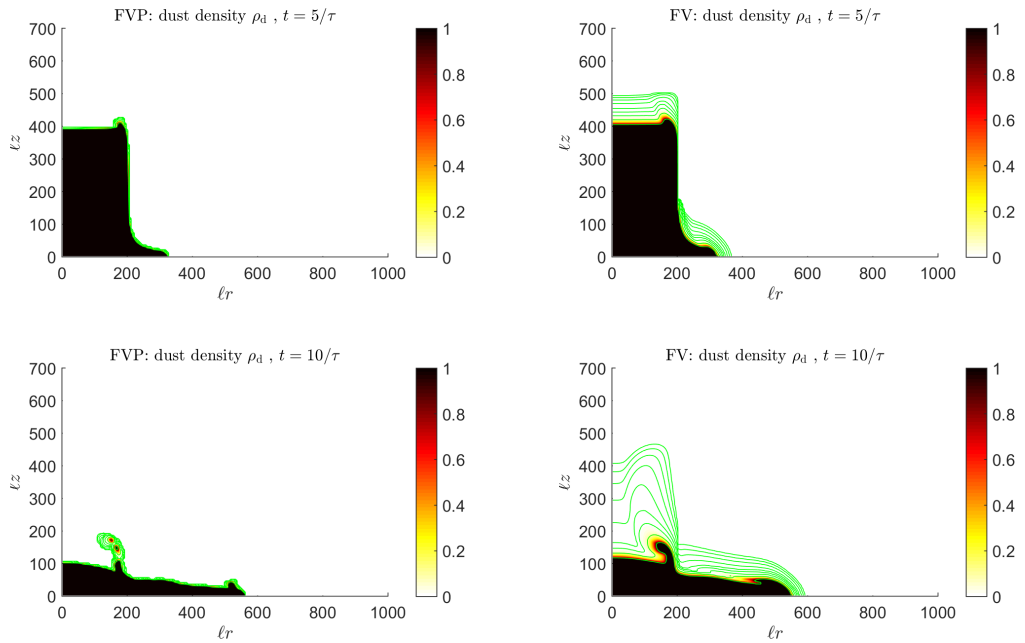

Figure 5.4. Example 3: The dust density at different times computed by the FVP (left column) and FV (right column) methods with resolution $N_r = 200, N_z = 140$. The green contour lines correspond to the densities 10^k, $k = -8, \ldots, 0$. The CPU time used for the FVP and FV results are $352s$ and $312s$, respectively.

Example 4—Volcanic eruption (with the redistribution of isolated particles). Next, we consider an example introduced in [45], which employs the dusty gas system (2.10) to simulate volcanic eruptions. The numerical experiment is conducted over the domain $(r,z)\in[0,1000/\ell]\times[0,700/\ell]$ and the initial conditions are given by

$$\rho_{\rm g}(r,z,0)=\frac{1}{\rho_{\rm ref}}(1.225-0.8559(11000-\ell z)),\ p_{\rm g}(r,z,0)=1+\frac{\mathfrak{g}}{p_{\rm ref}}(0.42795\ell z-9413.68)\ell z$$

and

$$\rho_{\rm d}(r,z,0)\equiv u_{\rm d}(r,z,0)\equiv v_{\rm d}(r,z,0)\equiv E_{\rm d}(r,z,0)\equiv u_{\rm g}(r,z,0)\equiv v_{\rm g}(r,z,0)\equiv 0,$$

that is, the initial condition is motionless and the dust phase is absent. Here, the initial gas density $\rho_{\rm g}(r,z,0)$ is, in fact, a linear approximation of the atmospheric gas density under the normal conditions and the initial gas pressure $p_{\rm g}(r,z,0)$ corresponds to a motionless steady state (2.16).

Free boundary conditions are implemented at the boundaries $r=1000/\ell$ and $z=700/\ell$, while reflective boundary conditions are set at the boundary $r=0$. The bottom boundary ($z=0$) consists of two segments: For $r\in(50/\ell,1000/\ell]$, a reflexive boundary condition is imposed, while for $r\in[0,50/\ell]$ we set:

$$(\rho_{\rm g},u_{\rm g},v_{\rm g},T_{\rm g},\rho_{\rm d},u_{\rm d},v_{\rm d},T_{\rm d})\big|_{r\in[0,50/\ell],z=0}=\left(\frac{9.9\times 10^4\,T_{\rm ref}}{1200\,p_{\rm ref}},0,\frac{80}{u_{\rm ref}},\frac{1200}{T_{\rm ref}},\frac{0.01\rho_{\rm p}}{\rho_{\rm ref}},0,\frac{80}{u_{\rm ref}},\frac{1200}{T_{\rm ref}}\right),$$

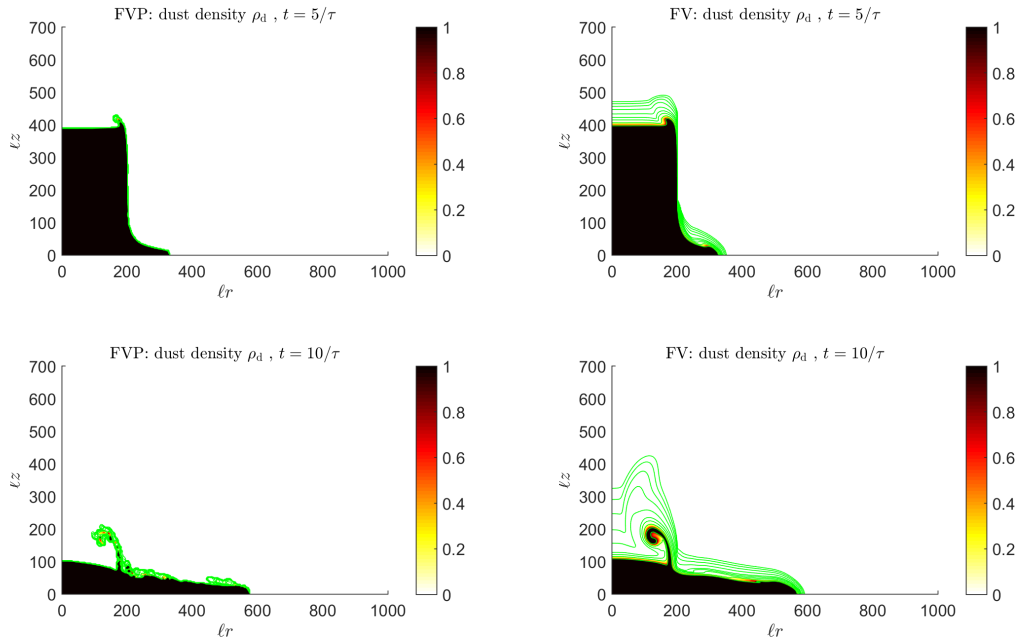

Figure 5.5. Example 3: The same as in Figure 5.4, but with $N_r = 400, N_z = 280$. The CPU time used for the FVP and FV results are 6183s and 2073s, respectively.

which simulates a volcano vent at the ground level, through which a hot mixture of dust and gas is injected into the computational domain.

In Figure 5.6, we show the dust density component of the solution at different times computed by the FVP method, and for the comparison, the FV results are shown in Figure 5.7. Here, for the FV method, a uniform grid with $N_r = 200, N_z = 140$ is used. For the FVP method, the same grid is employed for the computation of the gas phase, while the dust particles are injected into the computational domain from the aforementioned boundary vent in a manner that they are uniformly spaced with the horizontal distance $\Delta r/2$ and vertical distance Δz. The critical distance for particle merger was set as $d_{cr} = \Delta r/4$ in these computations. As one can see, more details are captured by the FVP method since the solutions obtained by the FV method are smoothened by the numerical diffusion. We also would like to point out that the FVP results are actually realized by a relatively small number of particles. At time $t = 50/\tau$, $M(50/\tau) = 24069$ particles are employed, which is less than the total number of FV cells $N_r \cdot N_z = 28000$.

Note that the point values of the dust density shown in Figure 5.6 are obtained using the reconstruction formula (5.2), which actually spreads the weights carried by each particle to its neighboring cells resulting in a smeared picture of the computed particle distribution. In Figure 5.8, we depict the dust density in the form of the particle distribution without using any point value reconstructions. Here, the ith particle is represented by a solid dot located at $(r_i^{\mathcal{P}}, z_i^{\mathcal{P}})$ with its area proportional to the weight $m_i r_i$. As one can see, the clustering effect of the dust phase is clearly captured by the FVP method, that is, some particles carry a much heavier weight than the other ones.

In order to compare the FVP and FV results, we show the dust density solution obtained by the FV method in Figure 5.9. Here, we plot the values $(\rho_{\text{d}})_{j,k}$ represented by solid dots of the size proportional to $\Delta r \Delta z\, r_j (\rho_{\text{d}})_{j,k}$ and located at the cell centers. Compared to the FVP results shown in Figure 5.8,

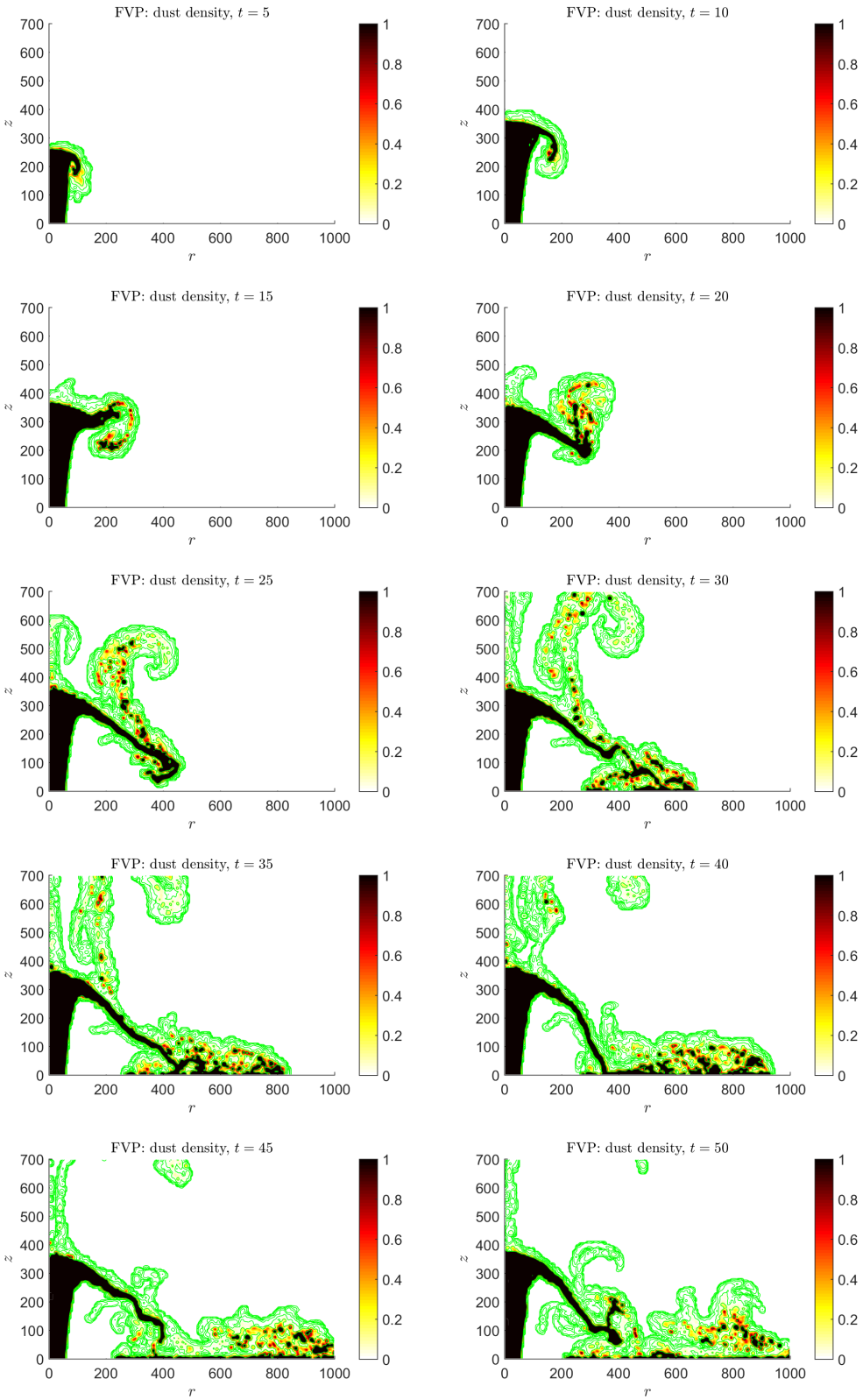

FIGURE 5.6. Example 4: The dust density at different times computed by the FVP method with resolution $N_r = 200, N_z = 140$. The green contour lines correspond to the densities 10^k, $k = -8, \ldots, 0$. The CPU time consumed is 8312s.

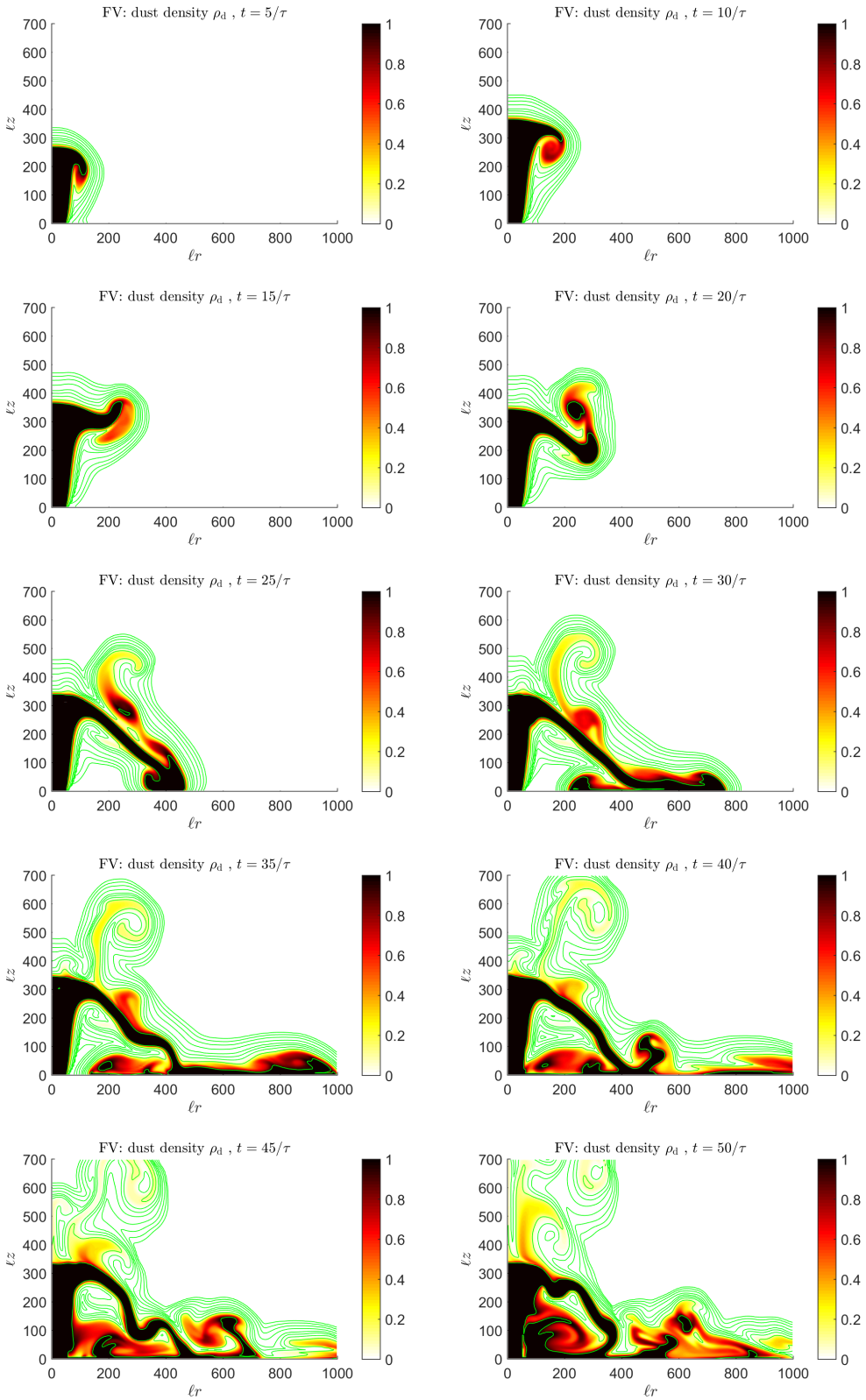

Figure 5.7. Example 4: The same as in Figure 5.6, but computed using the FV method. The CPU time consumed is 2276s.

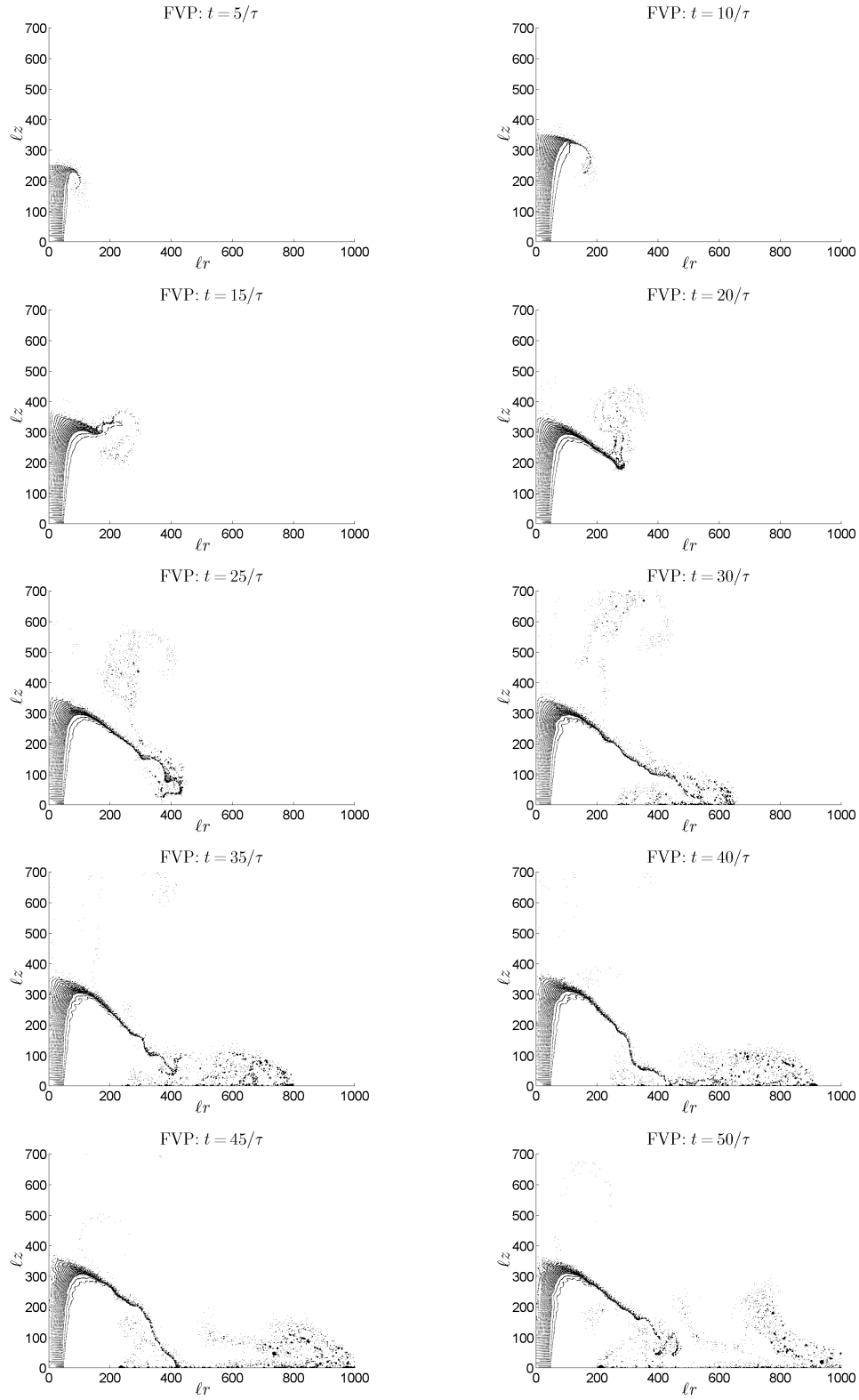

Figure 5.8. Example 4: The same as in Figure 5.6, but here the obtained particle distribution is represented by groups of solid dots located at $(r_i^{\mathcal{P}}, z_i^{\mathcal{P}})$ with its area proportional to the weight $m_i r_i$.

the FV results reflect the effect of numerical diffusion, that is, the dust clouds are characterized by a substantially smeared density profile.

Example 5—Volcanic eruption (without redistributing isolated particles). This example is devoted to exploring the results of the FVP methods implemented without any particle redistributions. As mentioned above, by adding the redistribution process introduced in §4.1.4 into the scheme we aim at capturing a smooth spreading of the dust mass and try to avoid the appearance of regions, which are filled with very small number the particles. However, a certain amount of numerical diffusion is artificially added through the redistribution process. Therefore, additional numerical experiments are needed to justify the effect of the redistribution.

We consider the same setting as in Example 4, but the redistribution process for the isolated particles is now turned off. As in Example 4, we depict the dust density solution obtained by the FVP methods in the following two ways: the recovered point values are plotted in Figure 5.10 and the particle distributions are represented by solid dots in Figure 5.11. Compared to the FVP results reported in Figures 5.6 and 5.8, the dust clouds in Figures 5.10 and 5.11 are represented by a smaller number of (in average) heavier particles. Though distinct in the dust clouds regions, both FVP schemes (with and without the redistribution process) are able to correctly capture the motions of the dust flows.

Example 6—Volcanic eruption with higher exit vent velocity (with and without redistribution isolated particles). In this last example, we consider the same setting as in Examples 4 and 5, except that we use a 2.5 times greater exit velocity $v_d = 200/u_{\text{ref}}$ and a larger computational domain $[0, 2000/\ell] \times [0, 4000/\ell]$ with $N_r = 160$ and $N_z = 320$.

The results obtained with and without redistribution of isolated particles are reported in Figures 5.12 and 5.13, respectively. As one can see from these figures, the redistribution procedure leads to a creation of larger groups of particles that show dusty cloud texture in greater details, compared with the ones obtained without any redistribution.

Unlike the results reported in Examples 4 and 5 and shown in Figure 5.11, the dusty gas column with a faster exit velocity reaches a greater altitude (about 2200 meters). After that, instead of collapsing, the column keeps buoyant and develops raising and expanding clouds with lower dust contents. The height and evolution of such jet structure show a good agreement with the results in [45].

Remark 5.2. We would like to point out that the numerical results reported in Examples 4–6 do not clearly suggest whether or not the redistribution process should be applied. A further study on the dust clustering process in the volcanic flows (including development of more realistic mathematical models, their numerical study and comparisons with observations) is definitely needed to draw a conclusion, but it is beyond the scope of the current paper.

Remark 5.3. We would like to emphasize that the data on the CPU times in Examples 3 and 4 are provided for illustration purposes only since the designed FVP and FV codes were not optimized for a fair CPU time comparison. In particular, an efficient implementation of the FVP method would require the development of fast summation and search techniques, which is left for future work. The purpose of showing the CPU times in this paper was to demonstrate that (i) for a given resolution, the FVP method would be more computationally expensive; (ii) the FVP method still outperforms the FV one since a much finer grid would be required for the FV method to achieve the results comparable to low resolution FVP computations.

Appendix A. Reconstruction Operator $\mathcal{R}$

In this section, we give a description of the procedures $\mathcal{R}$ used to reconstruct piecewise linear functions out of the corresponding grid functions.

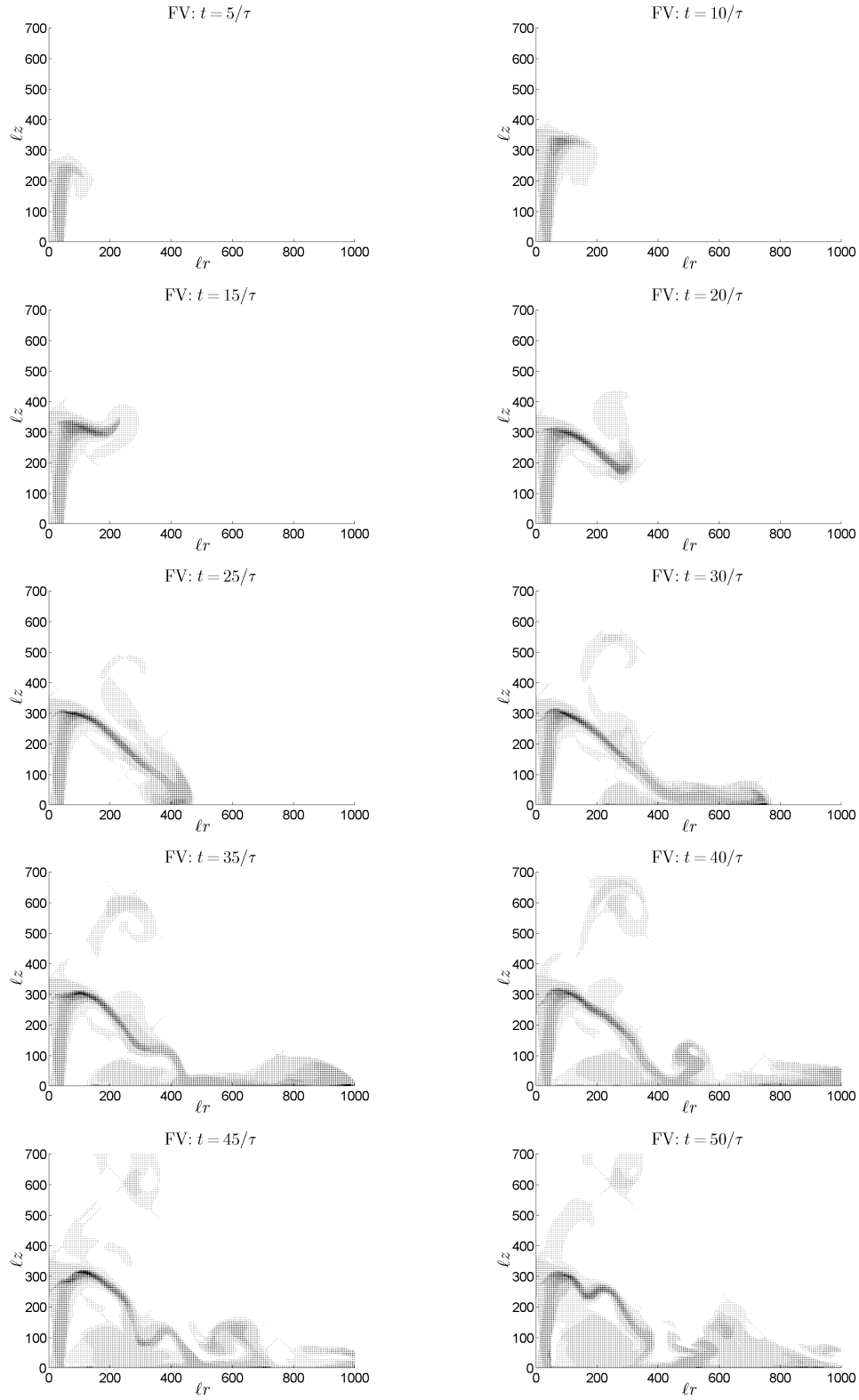

Figure 5.9. Example 4: The same as in Figure 5.7, but here the solution is represented by solid dots of the size proportional to $\Delta r \Delta z\, r_j (\rho_{\rm d})_{j,k}$ and located at the cell centers.

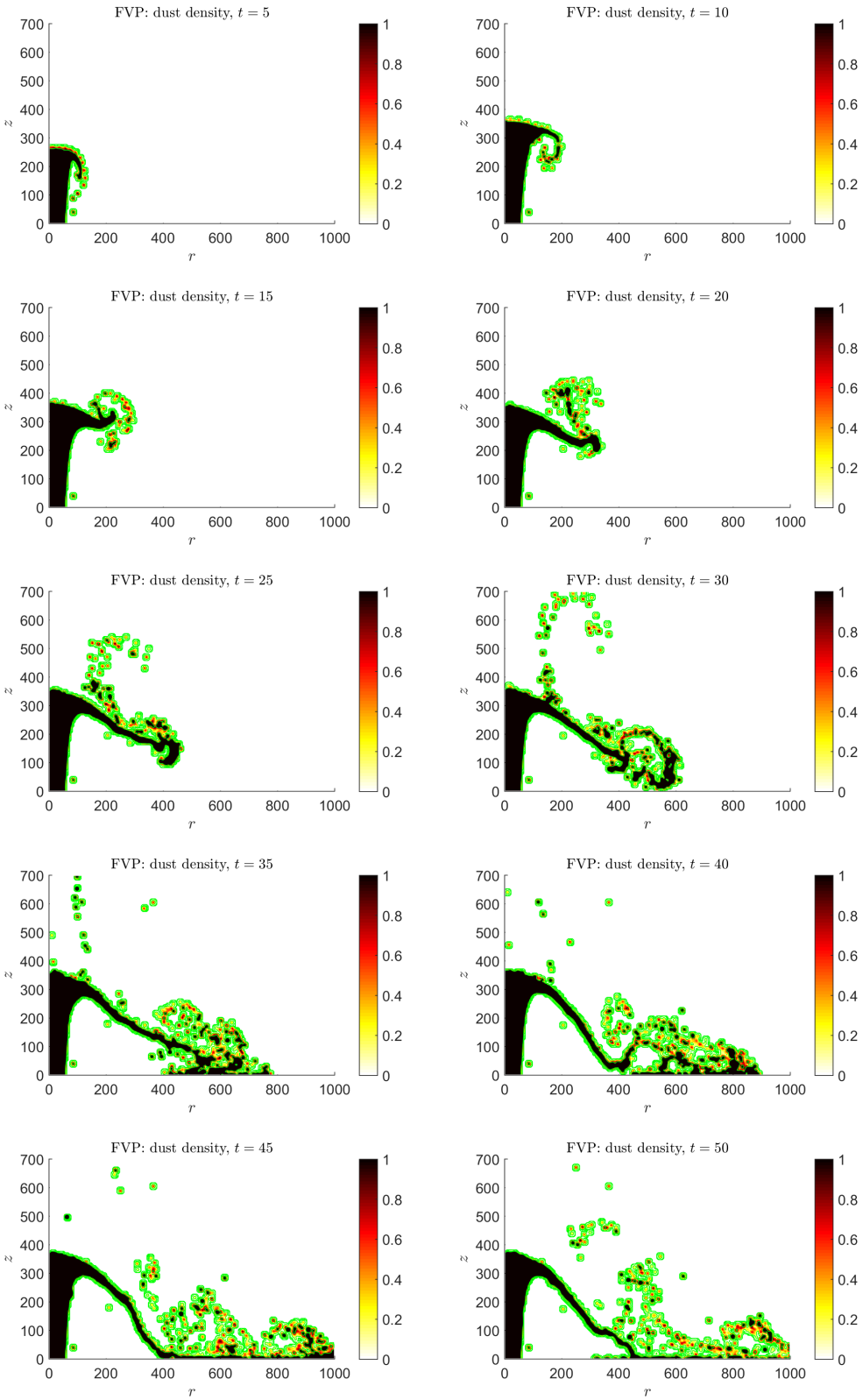

Figure 5.10. Example 5: The same as in Figure 5.6 but without isolated particle redistribution.

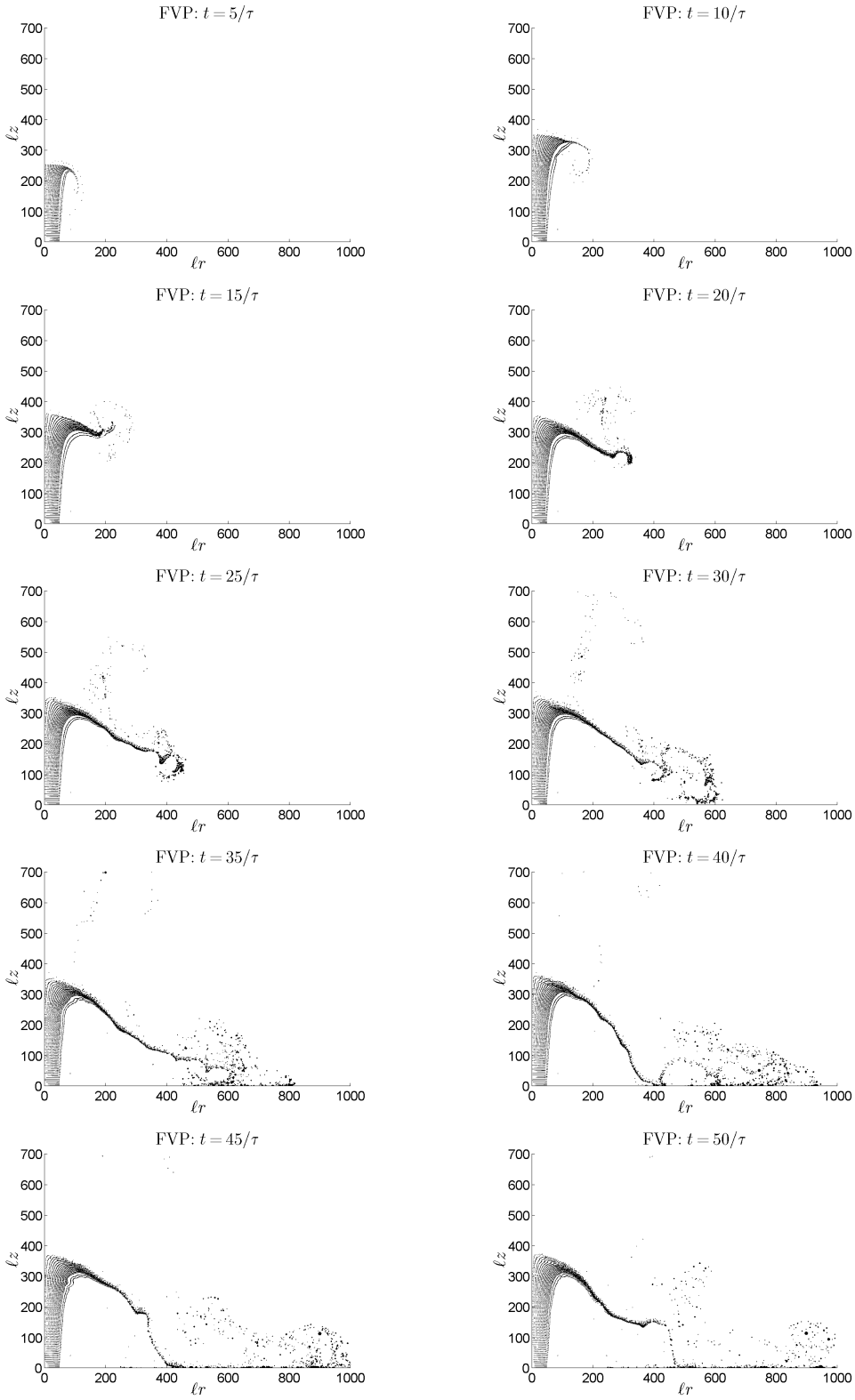

Figure 5.11. Example 5: The same as in Figure 5.8 but without isolated particle redistribution.

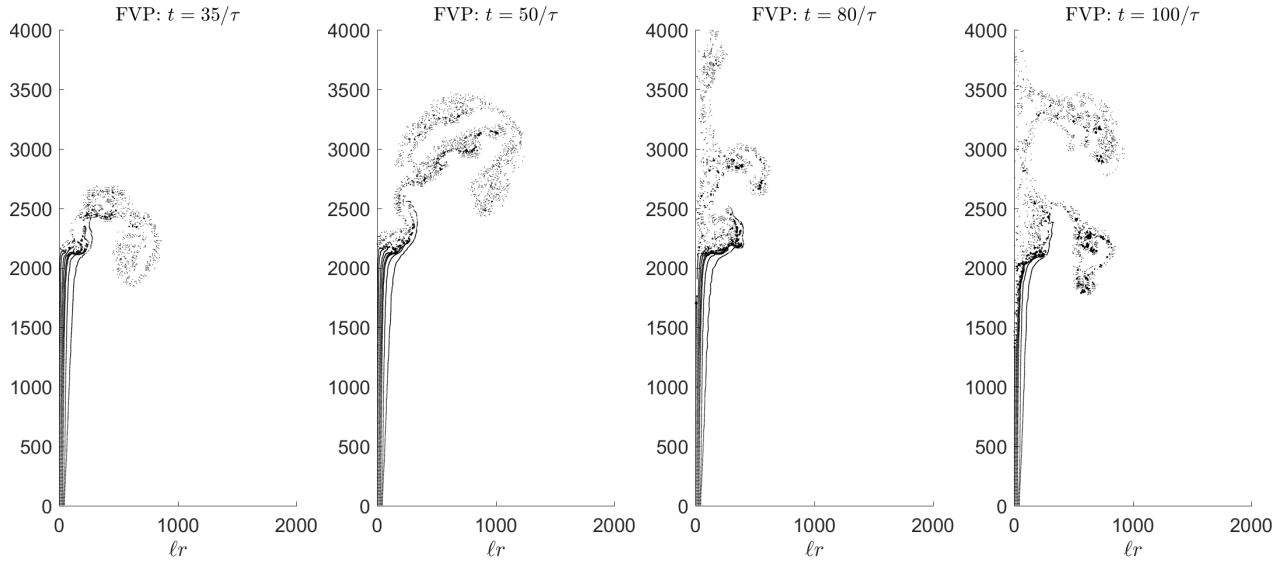

Figure 5.12. Example 6: The results obtained using the FVP method with redistributing isolated particles. The particles are represented by groups of solid dots located at $(r_i^{\mathcal{P}}, z_i^{\mathcal{P}})$ with its area proportional to the weight $m_i r_i$. At $t = 100/\tau$, the total number of particles is 10115 and the CPU time elapsed is 1321246.

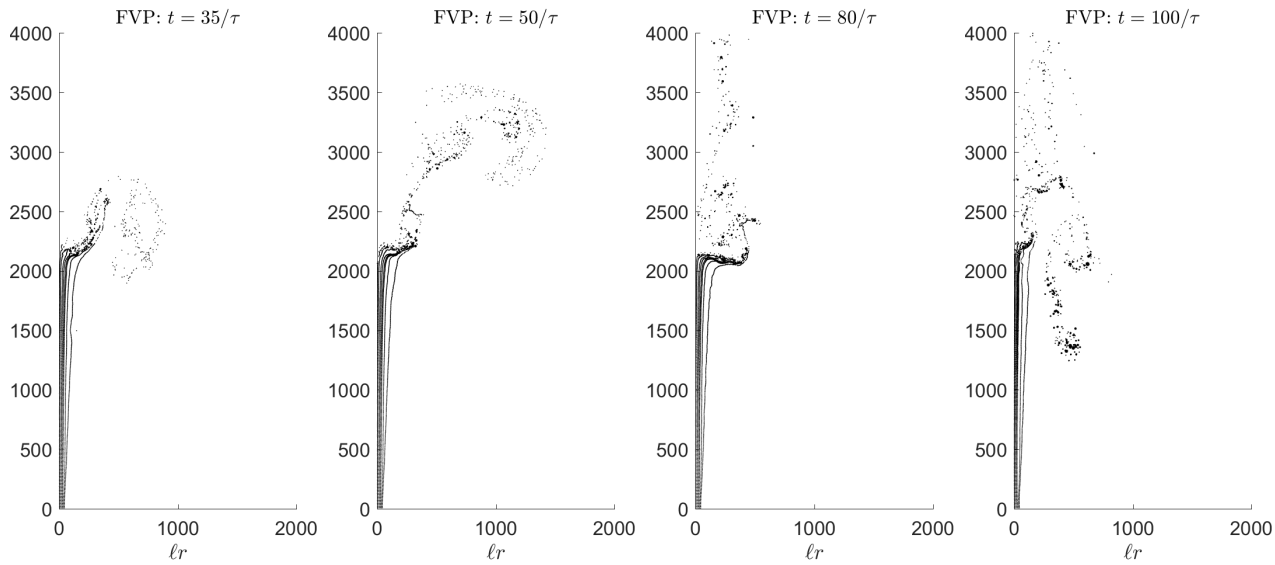

Figure 5.13. Example 6: The results obtained using the FVP method without redistributing isolated particles. The particles are represented by groups of solid dots located at $(r_i^{\mathcal{P}}, z_i^{\mathcal{P}})$ with its area proportional to the weight $m_i r_i$. At $t = 100/\tau$, the total number of particles is 2588 and the CPU time elapsed is 293369.

A.1. **One-Dimensional Case**

Given a set of values $\{\phi_j\}$ which are defined at cell centers $\{x_j\}$, a piecewise linear approximation of $\phi(x)$ is given by

$$\mathcal{R}\{\phi_j\}\big|_{x=\xi} := \sum_j \left[\phi_j + (\phi_x)_j(\xi - x_j)\right] \cdot \chi_{C_j}(\xi),$$

where χ_{C_j} is characteristic function of the interval C_j. To avoid oscillations, the slopes $(\phi_x)_j$ are to be computed using a nonlinear limiter. In all of the numerical experiments reported in §5, we have used a generalized minmod limiter (see, e.g., [38, 42, 54, 58]), that is,

$$(\phi_x)_j = \text{minmod}\left(\theta\,\frac{\phi_{j+1}-\phi_j}{\Delta x},\ \frac{\phi_{j+1}-\phi_{j-1}}{2\Delta x},\ \theta\,\frac{\phi_j-\phi_{j-1}}{\Delta x}\right),$$

where the minmod function is defined by

$$\text{minmod}(z_1, z_2, \ldots) := \begin{cases} \min(z_1, z_2, \ldots), & \text{if } z_i > 0\ \forall i, \\ \max(z_1, z_2, \ldots), & \text{if } z_i < 0\ \forall i, \\ 0, & \text{otherwise}, \end{cases} \tag{A.1}$$

and the parameter $\theta \in [1, 2]$ controls the amount of numerical dissipation: The use of larger values of θ typically leads to sharper, but more oscillatory numerical solution.

A.2. **Axisymmetric Three-Dimensional Case**

Given a set of values $\{\phi_{j,k}\}$ defined at cell centers (r_j, z_k), the operator $\mathcal{R}$ generates a piecewise linear function $\mathcal{R}\{\phi_{j,k}\}(r, z)$ defined over the entire computational domain:

$$\mathcal{R}\{\phi_{j,k}\}(r,z) := \sum_j\sum_k \left[\phi_{j,k} + (\phi_r)_{j,k}(r - r_{j,k}) + (\phi_z)_{j,k}(z - z_{j,k})\right] \cdot \chi_{C_{j,k}}(r,z), \tag{A.2}$$

where $\chi_{C_{j,k}}$ is characteristic function of the cell $C_{j,k}$. The slopes $(\phi_r)_{j,k}$ and $(\phi_z)_{j,k}$ are to be computed using a nonlinear limiter; see, e.g., [38, 42, 54, 58]. For example, one can use the generalized minmod limiter:

$$(\phi_r)_{j,k} = \text{minmod}\left(\theta\,\frac{\phi_{j+1,k}-\phi_{j,k}}{\Delta r},\ \frac{\phi_{j+1,k}-\phi_{j-1,k}}{2\Delta r},\ \theta\,\frac{\phi_{j,k}-\phi_{j-1,k}}{\Delta r}\right),$$
$$(\phi_z)_{j,k} = \text{minmod}\left(\theta\,\frac{\phi_{j,k+1}-\phi_{j,k}}{\Delta z},\ \frac{\phi_{j,k+1}-\phi_{j,k-1}}{2\Delta z},\ \theta\,\frac{\phi_{j,k}-\phi_{j,k-1}}{\Delta z}\right).$$

Appendix B. **Reconstruction Operator $\mathcal{R}^{\mathcal{P}}$**

In this section, we describe another reconstruction operator $\mathcal{R}^{\mathcal{P}}$, originally introduced in [14], which reconstructs a piecewise linear function from a set of point values prescribed at the centers of mass of particles located in each FV cell.

B.1. **One-Dimensional Case**

Given a set of values $\{\phi_j^{\text{CM}}\}$ defined at $\{x_j^{\text{CM}}\}$ introduced in (3.12), the reconstruction operator $\mathcal{R}^{\mathcal{P}}$ generates the following piecewise linear function:

$$\mathcal{R}^{\mathcal{P}}\{\phi_j^{\text{CM}}\}\big|_{x=\xi} := \sum_j \left[\,(\phi_j^{\text{CM}} + (\phi_x^{\text{CM}})_j(\xi - x_j^{\text{CM}})\right] \cdot \chi_{C_j}(\xi).$$

Here, the slopes $(\phi_x^{\mathrm{CM}})_j$ should be computed using a nonlinear limiter. In all of the 1-D numerical experiment shown in §5, we have used the minmod limiter introduced in (A.1):

$$(\phi_x^{\mathrm{CM}})_j = \mathrm{minmod}\left(\theta\,\frac{\phi_{j+1}^{\mathrm{CM}} - \phi_j^{\mathrm{CM}}}{x_{j+1}^{CM} - x_j^{CM}},\ \frac{\phi_{j+1}^{\mathrm{CM}} - \phi_{j-1}^{\mathrm{CM}}}{x_{j+1}^{CM} - x_{j-1}^{CM}},\ \theta\,\frac{\phi_j^{\mathrm{CM}} - \phi_{j-1}^{\mathrm{CM}}}{x_j^{CM} - x_{j-1}^{CM}}\right).$$

B.2. **Axisymmetric Three-Dimensional Case**

Given a set of values $\{\phi_{j,k}^{\mathrm{CM}}\}$ defined at $(r_{j,k}^{\mathrm{CM}}, z_{j,k}^{\mathrm{CM}})$ introduced in (4.12), the reconstruction operator $\mathcal{R}^{\mathcal{P}}$ generates the following piecewise linear function:

$$\mathcal{R}^{\mathcal{P}} i\{\phi_{j,k}\}(r,z) := \sum_j \sum_k \left[\phi_{j,k}^{\mathrm{CM}} + (\phi_r^{\mathrm{CM}})_{j,k}(r - r_{j,k}^{\mathrm{CM}}) + (\phi_z^{\mathrm{CM}})_{j,k}(z - z_{j,k}^{\mathrm{CM}})\right] \cdot \chi_{C_{j,k}}(r,z), \tag{B.1}$$

where $\chi_{C_{j,k}}$ is characteristic function of the cell $C_{j,k}$ and the slopes $(\phi_r^{\mathrm{CM}})_{j,k}$ and $(\phi_z^{\mathrm{CM}})_{j,k}$ are to be computed using a nonlinear limiter which can be applied as follows. We first take four planes, denoted by $\pi_{j,k}^{\mathrm{NE}}$, $\pi_{j,k}^{\mathrm{NW}}$, $\pi_{j,k}^{\mathrm{SE}}$, $\pi_{j,k}^{\mathrm{SW}}$, which are determined by the following four groups of points:

$$\begin{aligned}
\pi_{j,k}^{\mathrm{NE}} &: \{(r_{j,k}^{\mathrm{CM}}, z_{j,k}^{\mathrm{CM}}, \phi_{j,k}^{\mathrm{CM}}), (r_{j,k+1}^{\mathrm{CM}}, z_{j,k+1}^{\mathrm{CM}}, \phi_{j,k+1}^{\mathrm{CM}}), (r_{j+1,k}^{\mathrm{CM}}, z_{j+1,k}^{\mathrm{CM}}, \phi_{j+1,k}^{\mathrm{CM}})\},\\
\pi_{j,k}^{\mathrm{NW}} &: \{(r_{j,k}^{\mathrm{CM}}, z_{j,k}^{\mathrm{CM}}, \phi_{j,k}^{\mathrm{CM}}), (r_{j,k+1}^{\mathrm{CM}}, z_{j,k+1}^{\mathrm{CM}}, \phi_{j,k+1}^{\mathrm{CM}}), (r_{j-1,k}^{\mathrm{CM}}, z_{j-1,k}^{\mathrm{CM}}, \phi_{j-1,k}^{\mathrm{CM}})\},\\
\pi_{j,k}^{\mathrm{SE}} &: \{(r_{j,k}^{\mathrm{CM}}, z_{j,k}^{\mathrm{CM}}, \phi_{j,k}^{\mathrm{CM}}), (r_{j,k-1}^{\mathrm{CM}}, z_{j,k-1}^{\mathrm{CM}}, \phi_{j,k-1}^{\mathrm{CM}}), (r_{j+1,k}^{\mathrm{CM}}, z_{j+1,k}^{\mathrm{CM}}, \phi_{j+1,k}^{\mathrm{CM}})\},\\
\pi_{j,k}^{\mathrm{SW}} &: \{(r_{j,k}^{\mathrm{CM}}, z_{j,k}^{\mathrm{CM}}, \phi_{j,k}^{\mathrm{CM}}), (r_{j,k-1}^{\mathrm{CM}}, z_{j,k-1}^{\mathrm{CM}}, \phi_{j,k-1}^{\mathrm{CM}}), (r_{j-1,k}^{\mathrm{CM}}, z_{j-1,k}^{\mathrm{CM}}, \phi_{j-1,k}^{\mathrm{CM}})\},
\end{aligned} \tag{B.2}$$

respectively. We then denote the r- and z-slopes of the plane π by π_r and π_z and compute the slopes in (B.1) using the minmod function introduced in (A.1):

$$\begin{aligned}
(\phi_r^{\mathrm{CM}})_{j,k} &= \mathrm{minmod}\big((\pi_r)_{j,k}^{\mathrm{NE}}, (\pi_r)_{j,k}^{\mathrm{NW}}, (\pi_r)_{j,k}^{\mathrm{SE}}, (\pi_r)_{j,k}^{\mathrm{SW}}\big),\\
(\phi_z^{\mathrm{CM}})_{j,k} &= \mathrm{minmod}\big((\pi_z)_{j,k}^{\mathrm{NE}}, (\pi_z)_{j,k}^{\mathrm{NW}}, (\pi_z)_{j,k}^{\mathrm{SE}}, (\pi_z)_{j,k}^{\mathrm{SW}}\big).
\end{aligned} \tag{B.3}$$

Remark B.1. There may be cells in which no particles are located and, as the result, the cell averages of the reconstructed quantities are not available there. This however does not pose a problem since one only needs to use the operator $\mathcal{R}^{\mathcal{P}}$ to generate linear pieces in the cells where particles are present.

Remark B.2. As pointed out in [14], in the cases when one of the planes in (B.2) is perpendicular to the (r,z)-plane or not uniquely determined, the corresponding slopes are not taken account in (B.3).

References

[1] N. Botta, R. Klein, S. Langenberg, and S. Lützenkirchen. Well balanced finite volume methods for nearly hydrostatic flows. *J. Comput. Phys.*, 196(2):539–565, 2004.

[2] F. Bouchut. On zero pressure gas dynamics. In *Advances in kinetic theory and computing*, volume 22 of *Ser. Adv. Math. Appl. Sci.*, pages 171–190. World Sci. Publ., River Edge, NJ, 1994.

[3] F. Bouchut and F. James. Duality solutions for pressureless gases, monotone scalar conservation laws, and uniqueness. *Comm. Partial Differential Equations*, 24(11-12):2173–2189, 1999.

[4] F. Bouchut, S. Jin, and X. Li. Numerical approximations of pressureless and isothermal gas dynamics. *SIAM J. Numer. Anal.*, 41:135–158, 2003.

[5] Y. Brenier and E. Grenier. Sticky particles and scalar conservation laws. *SIAM J. Numer. Anal.*, 35:2317–2328, 1998.

[6] S. Carcano, L. Bonaventura, T. Esposti Ongaro, and A. Neri. A semi-implicit, second order accurate numerical model for multiphase underexpanded volcanic jets. *Geosci. Model Dev. Discuss.*, 6(1):399–452, 2013.

[7] P. Chandrashekar and C. Klingenberg. A second order well-balanced finite volume scheme for Euler equations with gravity. *SIAM J. Sci. Comput.*, 37(3):B382–B402, 2015.

[8] G.-Q. Chen and H. Liu. Formation of δ-shocks and vacuum states in the vanishing pressure limit of solutions to the euler equations for isentropic fluids. *SIAM J. Math. Anal.*, 34:925–938, 2003.

[9] A. Chertock, S. Cui, A. Kurganov, Ş. N. Özcan, and E. Tadmor. Well-balanced central-upwind schemes for the Euler equations with gravitation. Submitted.

[10] A. Chertock, S. Cui, A. Kurganov, and T. Wu. Well-balanced positivity preserving central-upwind scheme for the shallow water system with friction terms. *Internat. J. Numer. Meth. Fluids*, 78:355–383, 2015.

[11] A. Chertock and A. Kurganov. On a hybrid finite-volume particle method. *M2AN Math. Model. Numer. Anal*, 38:1071–1091, 2004.

[12] A. Chertock and A. Kurganov. On a practical implementation of particle methods. *Appl. Numer. Math.*, 56:1418–1431, 2006.

[13] A. Chertock, A. Kurganov, and G. Petrova. Finite-volume-particle methods for models of transport of pollutant in shallow water. *J. Sci. Comput.*, 27:189–199, 2006.

[14] A. Chertock, A. Kurganov, and Yu. Rykov. A new sticky particle method for pressureless gas dynamics. *SIAM J. Numer. Anal.*, 45:2408–2441, 2007.

[15] G.-H. Cottet and P. D. Koumoutsakos. *Vortex methods*. Cambridge University Press, Cambridge, 2000.

[16] S. Dartevelle, W. Rose, J. Stix, K. Kelfoun, and J.W. Vallance. Numerical modeling of geophysical granular flows: 2. Computer simulations of plinian clouds and pyroclastic flows and surges. *Geochem. Geophys. Geosyst.*, 5(8), 2004.

[17] V. Desveaux, M. Zenk, C. Berthon, and C. Klingenberg. A well-balanced scheme for the Euler equation with a gravitational potential. In *Finite volumes for complex applications. VII. Methods and theoretical aspects*, volume 77 of *Springer Proc. Math. Stat.*, pages 217–226. Springer, Cham, 2014.

[18] F. Dobran, A. Neri, and G. Macedonio. Numerical simulation of collapsing volcanic columns. *J. Geophys. Res.*, 98:4231–4259, 1993.

[19] J. Dufek and G. W. Bergantz. Dynamics and deposits generated by the Kos Plateau Tuff eruption: Controls of basal particle loss on pyroclastic flow transport. *Geochem. Geophys. Geosyst.*, 8(12), 2007.

[20] W. E, Yu. G. Rykov, and Ya. G. Sinai. Generalized variational principles, global weak solutions and behavior with random initial data for systems of conservation laws arising in adhesion particle dynamics. *Comm. Math. Phys.*, 177:349–380, 1996.

[21] B. Einfeld. On Godunov-type methods for gas dynamics. *SIAM J. Numer. Anal.*, 25:294–318, 1988.

[22] P. Glaister. Flux difference splitting for the Euler equations with axial symmetry. *J. Engrg. Math.*, 22(2):107–121, 1988.

[23] S. Gottlieb, D. Ketcheson, and C.-W. Shu. *Strong stability preserving Runge-Kutta and multistep time discretizations*. World Scientific Publishing Co. Pte. Ltd., Hackensack, NJ, 2011.

[24] S. Gottlieb, C.-W. Shu, and E. Tadmor. Strong stability-preserving high-order time discretization methods. *SIAM Rev.*, 43:89–112, 2001.

[25] M. Gurris, D. Kuzmin, and S. Turek. Finite element simulation of compressible particle-laden gas flows. *J. Comput. Appl. Math.*, 233(12):3121–3129, 2010.

[26] S. Hank, R. Saurel, and O. Le Metayer. A hyperbolic Eulerian model for dilute two-phase suspensions. *Journal of Modern Physics*, 2:997–1011, 2011.

[27] A. Harlow and A. A. Amsden. Numerical calculation of multiphase fluid flow. *J. Comput. Phys.*, 17:19–52, 1975.

[28] A. Harten, P. Lax, and B. van Leer. On upstream differencing and Godunov-type schemes for hyperbolic conservation laws. *SIAM Rev.*, 25:35–61, 1983.

[29] A. Kurganov and C.-T. Lin. On the reduction of numerical dissipation in central-upwind schemes. *Commun. Comput. Phys.*, 2:141–163, 2007.

[30] A. Kurganov, S. Noelle, and G. Petrova. Semi-discrete central-upwind scheme for hyperbolic conservation laws and Hamilton-Jacobi equations. *SIAM J. Sci. Comput.*, 23:707–740, 2001.

[31] A. Kurganov and G. Petrova. A second-order well-balanced positivity preserving central-upwind scheme for the Saint-Venant system. *Commun. Math. Sci.*, 5:133–160, 2007.

[32] A. Kurganov and E. Tadmor. New high resolution central schemes for nonlinear conservation laws and convection-diffusion equations. *J. Comput. Phys.*, 160:241–282, 2000.

[33] A. Kurganov and E. Tadmor. Solution of two-dimensional riemann problems for gas dynamics without Riemann problem solvers. *Numer. Methods Partial Differential Equations*, 18:584–608, 2002.

[34] M.-C. Lai and C. S. Peskin. An immersed boundary method with formal second-order accuracy and reduced numerical viscosity. *J. Comput. Phys.*, 160:705–719, 2000.

[35] R. J. LeVeque. The dynamics of pressureless dust clouds and delta waves. *J. Hyperbolic Differ. Equ.*, 1:315–327, 2004.

[36] R. J. LeVeque and D. S. Bale. Wave propagation methods for conservation laws with source terms. In *Hyperbolic problems: theory, numerics, applications, Vol. II (Zürich, 1998)*, volume 130 of *Internat. Ser. Numer. Math.*, pages 609–618. Birkhäuser, Basel, 1999.

[37] G. Li and Y. Xing. High order finite volume WENO schemes for the Euler equations under gravitational fields. *J. Comput. Phys.*, 316:145–163, 2016.

[38] K.-A. Lie and S. Noelle. On the artificial compression method for second-order nonoscillatory central difference schemes for systems of conservation laws. *SIAM J. Sci. Comput.*, 24(4):1157–1174, 2003.

[39] J. Luo, K. Xu, and N. Liu. A well-balanced symplecticity-preserving gas-kinetic scheme for hydrodynamic equations under gravitational field. *SIAM J. Sci. Comput.*, 33(5):2356–2381, 2011.

[40] H. Miura and I. I. Glass. On a dusty-gas shock tube. *Proc. R. Soc. Lond. Ser. A Math. Phys. Eng. Sci.*, 382(1783):373–388, 1982.

[41] A. Neri, T. E. Ongaro, G. Macedonio, and D Gidaspow. Multiparticle simulation of collapsing volcanic columns and pyroclastic flow. *J. Geophys. Res*, 108:1–22, 2003.

[42] H. Nessyahu and E. Tadmor. Nonoscillatory central differencing for hyperbolic conservation laws. *J. Comput. Phys.*, 87(2):408–463, 1990.

[43] B. Nilsson, O. S. Rozanova, and V. M. Shelkovich. Mass, momentum and energy conservation laws in zero-pressure gas dynamics and δ-shocks: II. *Appl. Anal.*, 90(5):831–842, 2011.

[44] B. Nilsson and V. M. Shelkovich. Mass, momentum and energy conservation laws in zero-pressure gas dynamics and delta-shocks. *Appl. Anal.*, 90(11):1677–1689, 2011.

[45] M. Pelanti and R. J. Leveque. High-resolution finite volume methods for dusty gas jets and plumes. *SIAM J. Sci. Comput.*, 28:1335–1360, 2006.

[46] C. S. Peskin. The immersed boundary method. *Acta Numer.*, 11:479–517, 2002.

[47] P.-A. Raviart. An analysis of particle methods. In *Numerical methods in fluid dynamics (Como, 1983)*, volume 1127 of *Lecture Notes in Math.*, pages 243–324. Springer, Berlin, 1985.

[48] Yu. G. Rykov. Propagation of singularities of shock wave type in a system of equations of two-dimensional pressureless gas dynamics. *Mat. Zametki*, 66:760–769 (Russian); translation in Math. Notes 66 (1999), pp. 628–635 (2000), 1999.

[49] Yu. G. Rykov. On the nonhamiltonian character of shocks in 2-d pressureless gas. *Boll. Unione Mat. Ital. Sez. B Artic. Ric. Mat.*, (8) 5:55–78, 2002.

[50] T. Saito. Numerical analysis of dusty-gas flows. *J. Comput. Phys.*, 176:129–144, 2002.

[51] B. Shotorban, G. B. Jacobs, O. Ortiz, and Q. Truong. An Eulerian model for particles nonisothermally carried by a compressible fluid. *Int. J. Heat Mass Transfer*, 65:845–854, 2013.

[52] C.-W. Shu and S. Osher. Efficient implementation of essentially non-oscillatory shock-capturing schemes. *J. Comput. Phys.*, 77:439–471, 1988.

[53] G. Strang. On the construction and comparison of difference schemes. *SIAM J. Numer. Anal.*, 5:506–517, 1968.

[54] P. K. Sweby. High resolution schemes using flux limiters for hyperbolic conservation laws. *SIAM J. Numer. Anal.*, 21(5):995–1011, 1984.

[55] C. T. Tian, K. Xu, K. L. Chan, and L. C. Deng. A three-dimensional multidimensional gas-kinetic scheme for the navier-stokes equations under gravitational fields. *J. Comput. Phys.*, 226(2):2003–2027, 10/1 2007.

[56] R. Touma, U. Koley, and C. Klingenberg. Well-balanced unstaggered central schemes for the Euler equations with gravitation. *SIAM J. Sci. Comput.*, 38(5):B773–B807, 2016.

[57] G. Valentine and K. Wohletz. Numerical models of Plinian eruption columns and pyroclastic. *J. Geophys. Res*, 94:1867–1887, 1989.

[58] B. van Leer. Towards the ultimate conservative difference scheme. V. A second-order sequel to Godunov's method. *J. Comput. Phys.*, 32(1):101–136, 1979.

[59] K. H. Wohletz, T. R. McGetchin, M. T. Sandford II, and E. M. Jones. Hydrodynamic aspects of caldera-forming eruptions: numerical models. *J. Geophys. Res*, 89:8269–8285, 1984.

[60] Y. Xing and C.-W. Shu. High order well-balanced WENO scheme for the gas dynamics equations under gravitational fields. *J. Sci. Comput.*, 54(2-3):645–662, 2013.

[61] K. Xu, J. Luo, and S. Chen. A well-balanced kinetic scheme for gas dynamic equations under gravitational field. *Adv. Appl. Math. Mech.*, 2:200–210, 2010.

[62] M. Yuen. Some exact blowup solutions to the pressureless Euler equations in $\mathbb{R}^N$. *Commun. Nonlinear Sci. Numer. Simul.*, 16(8):2993–2998, 2011.